TMPRSS2 reduces antibody recognition of SARS-CoV-2 spike

Andrea Cottignies-Calamarte[1, 2], Alejandro De Cruz[1, 2], Cyril Planchais[3], Françoise Porrot[2], Mateo Kryzpow[1, 2], Martin Jungbauer-Groznica[1, 2], Eva Thuillier[2], Amelie Willeveau[2], Isabelle Staropoli[2], Florence Guivel-Benhassine[2], Pierre Rosenbaum[3], Ignacio Fernández[4], Felix Rey[4], Julian Buschrieser[2], Sophie Trouillet-Assant[6,7], Hugo Mouquet[3], Olivier Schwartz[2,5], Timothée Bruel[1, 2,5,*]

1: *Institut Pasteur, Université Paris Cité, Antiviral Activities of Antibodies Group, Paris, France*

2: *Institut Pasteur, Université Paris Cité, Virus and Immunity Unit, Paris, France*

3: Institut Pasteur, Université Paris Cité, Humoral Immunology Unit, Paris, France

4: *Institut Pasteur, Université Paris Cité, Structural Virology Unit, CNRS UMR 3569 Paris, France*

5: *Vaccine Research Institute, Créteil, France*

6: CIRI-Centre International de Recherche en Infectiologie, Université Claude Bernard Lyon 1, Inserm, U1111, CNRS, UMR5308, ENS Lyon, Université Jean Monnet de Saint-Etienne, Lyon, 69007, France.

7 : Joint Research Unit Civils Hospices of Lyon-bioMérieux, Hospices Civils de Lyon, Hôpital Lyon Sud, Pierre-Bénite, 69310, France.

[*]: corresponding authors: timothee.bruel@pasteur.fr

Abstract

The serine protease TMPRSS2 acts as a cofactor for SARS-CoV-2 entry by cleaving the viral spike (S) to initiate fusion. Whether TMPRSS2 has an impact on humoral immune response against S remains poorly characterized. Here, we show that TMPRSS2 impairs antibody binding to S. In S-expressing and infected cells, TMPRSS2 decreases monoclonal antibody (mAb) and immune serum binding, as well as antibody-dependent cellular cytotoxicity (ADCC) induction. Using a panel of 39 mAbs targeting various S regions, we observe that those binding to the S2 subunit are the most affected by TMPRSS2. TMPRSS2 promotes a partial shedding of S1 and changes S2 conformation. This processing reduces Angiotensin-Converting Enzyme 2 (ACE2) binding while increasing cell-cell fusion. We further observe that the capacity of TMPRSS2 to decrease antibody recognition is conserved across coronaviruses and shared with other TMPRSS proteins. However, TMPRSS2 expression in infected cells does not impact significantly virions' infectivity or the antibody recognition, as measured by flow virometry. Collectively, our findings suggest that TMPRSS2 processing of S favors a fusion intermediate conformation which is less sensitive to antibody recognition.

Introduction

The SARS-CoV-2 Spike (S) is a trimeric glycoprotein, responsible for viral fusion. Each protomer is composed of two subunits, S1 and S2, separated by a furin cleavage site (FCS). The S1 subunit comprises the receptor binding domain (RBD), which interacts with the cellular receptor Angiotensin-Converting Enzyme 2 (ACE2), and the N-terminal domain (NTD) (Hoffmann et al., 2020). S2 encompasses the fusion machinery and the transmembrane domain (Hills et al., 2025; Lusvarghi et al., 2025; Marcink et al., 2022; Zhang et al., 2025). Interaction between the RBD and ACE2 leads to S1 shedding and unmasking of the S2 fusion peptide (FP) (Grunst et al., 2024; Lusvarghi et al., 2025; Marcink et al., 2022). Insertion of the FP within the target membrane requires a proteolytic cleavage in a second site within S2, named S2', which is remarkably conserved across coronaviruses. Processing of the S2' site occurs at the plasma membrane or in endosomes, by transmembrane serine protease 2 (TMPRSS2) or cathepsins, respectively (Kakizaki et al., 2024). TMPRSS2 may also process S at the FCS site, as furin proteases and TMPRSS2 cleavage signals overlap (R–X–[K/R]–R↓ and [K/R]↓-S, respectively) (Fraser et al., 2022). Other members of the TMPRSS family can process S protein at S1/S2 and S2' sites, albeit with variable efficacy (Kishimoto et al., 2021; Zang et al., 2020). Proteolytic cleavage by TMPRSS2, and possibly other proteases, may occur outside of the canonical S1/S2 and S2' sites with functional consequences that remain largely misunderstood (Fraser et al., 2022; Lusvarghi et al., 2025; Meng et al., 2022). Thus, cellular proteases shape SARS-CoV-2 S protein structure and function.

Despite intracellular assembly and budding of viral particles, SARS-CoV-2-infected cells express S at the plasma membrane due to leaky coatomer interaction (Dey et al., 2022). If neighboring cells express ACE2 it may lead to syncytia formation, where TMPRSS2 appears to be dispensable though it accelerates the process (Buchrieser et al., 2020; Cattin-Ortolá et al., 2021). Membrane-bound S expression also enables the clearance of infected cells via antibody Fc-mediated functions, such as ADCC (Dufloo et al., 2021; Guenthoer et al., 2024), which may participate in the protection mediated by non-neutralizing anti-S antibodies (Clark et al., 2024). Yet, the main correlate of protection against COVID-19 is antibody neutralization (Earle et al., 2021; Goldblatt et al., 2022; Khoury et al., 2021). The most potent neutralizing antibodies target the RBD, although antibody responses are also elicited against other S regions (Bean et al., 2025; Clark et al., 2024; Guenthoer et al., 2024; Ju et al., 2020; Pinto et al., 2020; Planchais et al., 2022; Zhou et al., 2023; Zost et al., 2020). Both vaccination and infection elicit neutralizing antibodies, but the emergence of immune-evasive variants enables viral circulation in immune

populations (Dufloo et al., 2021; Guenthoer et al., 2024; Natarajan et al., 2021; Ng et al., 2022, 2021; Planchais et al., 2022; Sterlin et al., 2021). Consequently, the SARS-CoV-2 pandemic is characterized by sequential waves of immune-evasive variants (Jian et al., 2024; Planas et al., 2024, 2022, 2021). Viral immune escape is mostly driven by mutations in key neutralizing epitopes. Other mechanisms, such as differential glycosylation and reduced S exposition by infected cells, also contribute to SARS-CoV-2 evasion of humoral immune responses (Boson et al., 2021; Kim et al., 2023; Sztain et al., 2021). Characterizing those alternative antibody evasion strategies requires an in-depth understanding of S-antibody interactions. The S adopts various conformation (closed, opened, pre-fusion, post-fusion), which are not all equally recognized by antibodies. Structural approaches have extensively characterized extreme states (i.e. stabilized pre- and post-fusion trimers), but the landscape of intermediate conformations and their sensitivity to antibody is poorly characterized. The extend to which some of those conformations may contribute to antibody evasion is also unknown.

In this study, we hypothesize that the processing of SARS-CoV-2 S by TMPRSS2 will modify its recognition by antibodies. We observe that proteolytic cleavage of S by TMPRSS2 reduces antibody binding at the surface of infected cells. Not all antibodies are affected similarly, with those targeting S2 being the most sensitive. We further determine that TMPRSS2 rearranges S conformation to reduce antibody binding and ADCC induction against S-expressing cells while preserving S fusogenicity. In contrast, on viral particles, TMPRSS2 only moderately reduced antibody binding. Altogether, our results demonstrate that TMPRSS2 changes S conformation to impair antibody recognition and ADCC during SARS-CoV-2 infection, shedding light on a novel pro-viral role of this protease.

Methods

Antibodies and chemicals

Anti-SARS-CoV-2 spike monoclonal antibodies (mAbs) were produced in vitro as previously described (Planchais et al., 2022). Briefly, cDNA encoding for heavy and light antibody chains were either generated in-house from S-specific memory B cells (Planchais et al., 2024, 2022) or obtained from public sequences. All mAbs were produced as human IgG1 by co-transfection of 293-Freestyle (ThermoFisher), followed by affinity purification with protein G Sepharose 4 fast flow beads (GE Healthcare) and validated by ELISA for antigen specificity (Planchais et al., 2022). See **Table 1** for a detailed characterization of mAbs. TMPRSS2 staining was performed with an anti-TMPRSS2 nanobody described previously (Saunders et al., 2023). Hygromycin, puromycin and blasticidin were obtained from InvivoGen.

Human sera

Serum of individuals with hybrid immunity (Wuhan infection followed by 3 mRNA vaccine doses; **Table 2**) were obtained in the framework of the Covid-Ser cohort. A written informed consent was obtained from all participants; ethics approval was obtained from the national review board for biomedical research in April 2020 (Comité de Protection des Personnes Sud Méditerranée I, Marseille, France; ID RCB 2020-A00932-37; NCT04341142).

Plasmids

SARS-CoV-2 spikes from D614G, Delta, BA.4/5, BQ1.1, XBB.1.5/9, EG.5.1, XEC, and KP3.1.1 were human codon-optimized and synthetized (GeneArt, Thermo Fisher Scientific) as described (Buchrieser et al., 2020). Downstream cloning was performed using the Gateway strategy (ThermoFisher) in phCMV and pLV-EF1a-IRES-Puro or Hygro (Addgene #85132 and #85134). Expression plasmid were all previously described: Myc- or mScarlet-I-tagged TMPRSS in pCAGS or pCDEST respectively (Hoffmann et al., 2021; Saunders et al., 2023), S from coronaviruses 229E, RatG13 and NL63 in pcDNA3 (Ng et al., 2022), pVAX expressing S-BANAL20-236 (Temmam et al., 2022), lentivector plasmid pLV-ACE2 (Buchrieser et al. 2020) and pQCXIP-GFP1-10 and pQCXIP-GFP11 (Addgene #68716 and #68715, respectively). All sequences were confirmed by sequencing (Eurofins Genomics). VSV-G pseudovirus vectors were produced by phosphate calcium transfection as previously described (Buchrieser et al., 2019).

Cells

134 HEK293T, IGROV-1 and Caco2 cells were obtained from ATCC and maintained in DMEM
135 glutamax (Gibco) containing 10% heat-inactivated FCS (Gibco) and 1% Penicilin-
136 Streptomycin (Gibco). The absence of mycoplasma was monitored weekly using the MycoAlert
137 kit (Lonza). Mucilair® primary human nasal epithelial cells (hNECs) were purchased from
138 Epithelix (Switzerland). 293T-S and IGROV-1-TMPRSS2 were cultivated in presence of
139 1µg/ml puromycin or 250 µg/ml hygromycin, respectively, to maintain transgene expression.
140 Caco2-S were generated by lentiviral transduction and selected with 1µ/ml puromycin 4-5 days
141 before each experiment, because of the cytotoxicity of S in those ACE2-expressing cells. CD16
142 reporter Jurkat cell line was cultivated as per the manufacturer recommendations (Promega).
143 The SARS-CoV-2 reporter cells S-Fuse (293T-GFP1-10 and 293T-GFP11) and IGROV-1-
144 TMPRSS2 were previously described and maintained accordingly (Buchrieser et al., 2020,
145 2019; Planas et al., 2024).
146
147 **Viral production, titration and cell infection**
148 Amplification and production of SARS-CoV-2 D614G and XBB.1.5 variants have been
149 previously described (Planas, 2024). For S surface staining, 10^6 Caco2, IGROV-1 (WT or
150 TMPRSS2+) were plated in 6-wells plate. The next day, cells were infected with D614G or
151 XBB1.5 variants for 2h in fresh media, after what media was changed. At 24h post-infection
152 (hpi), Caco2 cells were either treated with Camostat (SigmaAldrich) or DMSO containing
153 media and incubated for another 24h. IGROV-1 cells were infected for 48h. After infection,
154 cells were washed 2 times in PBS EDTA and detached with trypsin before transferring to 96-
155 wells plate for spike staining as described in the staining section. After fixation, cells were
156 permeabilized for staining with Dylight488 anti-nucleocapsid (N) mouse IgG1 (in-house
157 production). For D614G production in IGROV-1 WT or overexpressing TMPRSS2, $2x10^6$,
158 cells were plated the day before infection in a T25 flask (Greiner). The next day, cells were
159 infected and inoculum was replaced with fresh media after 2h. Supernatant was harvested at 2-
160 and 3-days post-infection (dpi) and clarified at 1000g for 10min before storage at -80°C.
161 Samples were incubated 10min at 80°C before quantifying N gene in the supernatants using the
162 Luna universal RT-qPCR kit (New-England Biolab), the N2 primers tandem (Lu et al., 2020)
163 and analyzed using a QS6 pro (ThermoFisher), as reference to a commercial standard (Sigma,
164 EURM-001).
165
166 **Transfection**

167 For TMPRSS2 transfection, 10^6 cells in 3ml DMEM 10%FCS were plated in 6-wells plate and
168 transfected with 1 µg plasmid DNA in 1ml Optimem (Gibco) and 12 µl Lipofectamin2000
169 (ThermoFisher). In multiple transfection conditions, 6.10^5 cells were plated in 150 µl DMEM
170 10% FCS onto which 50µl Optimem containing 100ng DNA and 0.6 µl Lipofectamin2000 were
171 added. Transfection lasted overnight before any downstream analysis or assay.
172
173 **Antibody binding analysis by flow cytometry**
174 Cells were detached in PBS 1%EDTA or 0.05% trypsin (Gibco) and washed before staining
175 with 1µg/ml final antibody concentration for 15min at 4°C in DMEM 10% FCS. Sera were used
176 at a dilution of 1:100 in DMEM 10%FCS. Cells were then washed in PBS before staining with
177 a goat anti-human IgG AlexaFluor 647 (Invitrogene) for 15min at 4°C, washed in PBS and
178 stained with Fixable Aqua Dead cells (ThermoFisher) for 10min at 4°C. Next, cells were
179 washed in DMEM 10%FCS and cells were fixed in PBS-4%PFA (ThermoFisher) for 15min
180 before a final PBS wash. Flow cytometry analysis was performed on Attune machine
181 (ThermoFisher) and analyzed on FlowJo V10.10.0 (BD Life Science). When indicated %
182 reduction in binding was calculated based on the mean fluorescence intensity (MFI) as follows
183 $\left(1 - \frac{MFI(Ab\ upon\ TMPRSS\ transfection)}{MFI(Ab\ upon\ pEmpty\ transfection)}\right) \times 100\%$
184
185 **S1 ELISA**
186 Supernatants were centrifuged 5min 1.000g before storage at -20°C. Anti-NTD antibody
187 Cv2.1169 was coated overnight in PBS at 5µg/ml onto 96 well plate (Corning #3361). Samples
188 were diluted in PBS 5% FCS and incubated for 2h at 37°C after plating. Anti-RBD antibody
189 SA55-biotinylated was diluted in PBS 5% FCS and incubated for 1h at 37°C, followed by
190 streptavidin-HRP (BD, #554066, diluted 1000 times). Detection was performed using OPD
191 (Sigma) and stopped using 3M sulfuric acid. Between each step, plates were thoroughly washed
192 with PBS.
193
194 **Donor-Acceptor spike-mediated fusion**
195 $5x10^5$ 293T-S cells expressing GFP1-10 were cocultured in a 1:1 ratio with 293T-GFP11 stably
196 expressing ACE2 or not in µClear black 96-well plate (Greiner Bio-One). Cells were incubated
197 for 4h before fixation in 4% PFA final. Plates were then washed and nuclei were stained in
198 PBS-Hoechst 33342 (Invitrogen; diluted 10.000 times) and images were acquired using the
199 Opera Phenix High-Content Screening System (PerkinElmer). GFP area per well was

200 calculated using Harmony 191 High-Content Imaging and Analysis Software (PerkinElmer,
201 HH17000012, v.5.0). Normalized GFP area was calculated by dividing GFP area of the tested
202 condition by GFP area observed in the absence of any TMPRSS2 transfection.
203
204 **ADCC assay**
205 $5x10^5$ transfected 293T-S-D614G were plated in white 96-wells plates with 100-fold diluted
206 serum and $5x10^5$ CD16 reporter Jurkat cells for 24h at 37°C. CD16 activation was then
207 measured by firefly Luciferase using Bright-Glo (Promega) and an Enspire plate reader (Perkin-
208 Elmer). Luminescence signal of each well was normalized over the luminescence measured for
209 the coculture of 293T-S-D614G and Jurkat CD16 NFAT Luc in the absence of sera.
210
211 **S-fuse neutralization assay**
212 The day before the assay, 16.10^3 S-Fuse cells (8.10^3 U2OS-ACE2-GFP1-10 & 8.10^3 U2OS-
213 ACE2-GFP11) were plated in µClear black 96-well plate. The next day, the virus was incubated
214 with serum or antibody dilutions in DMEM 10%FCS 1%PS for 15min and was added to the
215 cells. Plates were incubated for 18h and fixed with PFA 4%. Plates were then washed and
216 stained with Hoechst 33342. Images were acquired using the Opera Phenix High-Content
217 Screening System (PerkinElmer). GFP area, number GFP and DAPI objects per well were
218 determined using Harmony 191 High-Content Imaging and Analysis Software (PerkinElmer,
219 HH17000012, v.5.0).
220
221 **Flow virometry**
222 Virus suspensions were stained with Syto24 (ThermoFisher S7559, 20µM final) and indicated
223 antibodies (1 µg/ml diluted in PBS) for 15min at room temperature. Next, a goat anti-human
224 IgG AlexaFluor 647 (1µg/ml final) was added to the mix and incubated for another 15min.
225 Finally, an equal volume of PFA 4% was added for 15min before further diluting sample in
226 0.02µm-filtered PBS and analyzed with the Cytoflex Nano (Beckman Coulter) and FlowJo.
227
228 **Statistical analysis**
229 Graphpad Prism V10.6.1 was used for statistical analysis.
230
231

232 **Results**

233 *TMPRSS2 impairs antibody binding to membrane-bound spike*

234 To investigate the impact of TMPRSS2 on the binding of anti-S mAbs, we transfected
235 293T cells stably expressing the D614G S protein (293T-S-D614G) with TMPRSS2-mScarlet-
236 I (**Fig. 1A**) and stained them with either Cv2.9116 (pan-coronavirus anti-S2) or S309 (anti-
237 RBD; parental version of sotrovimab). Flow cytometry analysis revealed that TMPRSS2
238 expression reduced significantly the median fluorescence intensity (MFI) of both mAbs by 73%
239 and 40%, respectively (respective ranges 74,7%-81,4% and 40,5%-45%, **Fig. 1B** and **1C**). The
240 catalytically inactive TMPRSS2 mutant S441A (TMPRSS2 S441A) does not reduce mAbs
241 binding (**Fig. 1B** and **1C**). Treatment of TMPRSS2-transfected 293T-S-D614G with the
242 TMPRSS2 inhibitor camostat resulted in an increase of the MFI of both Cv2.9116 and S309
243 (**Fig. S1A**). In the same conditions, the MFI of an anti-MHC-I mAb (clone W6/32) is not
244 decreased by TMPRSS2 (**Fig. S1B**).

245

246 Then, we generated Caco2-S-D614G cells and treated them with 1000 µM camostat (a
247 broad serine-proteases inhibitor) 24h before staining with Cv2.9116 and S309 (**Fig. S1C**). The
248 ability of both mAbs to bind to Caco2-S-D614G was increased by camostat from 31 to 34%
249 and from 76 to 81% for Cv2.9116 and S309, respectively. We further infected Caco2 cells with
250 SARS-CoV-2 (variants D614G and XBB.1.5) for 24h before adding Camostat and quantified
251 the binding of anti-spike Cv2.9116 and S309 (**Fig. 1D, S1E** and **Fig. S1D**). Camostat treatment
252 increased the binding of Cv2.9116 to infected cells from 54% to 78% and from 8,2% to 25%,
253 on D614G and XBB.1.5-infected cells, respectively. S309 binding was increased only against
254 XBB.1.5 (from 76% to 81%; Fig. **S1E**). We also infected IGROV-1 cells overexpressing
255 TMPRSS2 with D614G and XBB.1.5 variants and observed a reduction in Cv2.9116 and S309
256 binding as compared to WT cells (**Fig. 1E, Fig. S1F** and **S1G**).

257

258 Finally, we used flow cytometry to compare TMPRSS2 levels across the different cellular
259 systems, including the gold standard human nasal epithelial cells differentiated at the air-liquid
260 interface (hNEC-ALI) model, which express physiological levels of TMPRSS2 (**Fig. S1H**).
261 Transfected 293T cells express the highest levels of TMPRSS2 and Caco2 cells express the
262 lowest and hNEC-ALI cells express intermediate levels (**Fig. S1H**). Overall, our data show that
263 TMPRSS2 decreases the binding of anti-S mAbs to S-expressing and infected cells. This effect
264 relies on the catalytic activity of TMPRSS2 and is specific to S.

265

266 *Anti-S2 antibodies exhibit an increased sensitivity to TMPRSS2-mediated evasion*

267 We next investigated whether TMPRSS2 decreases the binding of different mAbs
268 equally. To this end, we used a panel of 39 mAbs recognizing different region on S ectodomain
269 **(Table 1)**. Over-expression of TMPRSS2 in 293T-S-D614G (**Fig. 2A**) and 293T-S-BA.5 (**Fig.**
270 **S2A**) cells decreases the binding of all tested mAbs. Anti-RBD mAbs show an average
271 36,1±2,6% decrease in binding upon TMPRSS2 expression, regardless of their RBD class **(Fig.**
272 **2B and 2C)**. Among anti-S2 mAbs, TMPRSS2 expression decreases the binding of anti-FP and
273 non-FP mAbs by 46±7% and 72,9±3,5%, respectively. Similarly, not all NTD epitopes behave
274 in the same way, with a larger binding decrease observed for supersite rather than non-supersite
275 mAbs (55,3±12,5% vs 31,6±3,1%). The reduction in binding upon TMPRSS2 expression
276 negatively correlates with binding intensity in the absence of TMPRSS2 **(Fig. 2D)**. This
277 analysis highlights the epitope specificity of TMPRSS2-mediated antibody evasion, as the
278 group that is strongly impacted is composed of anti-S2 (both FP and non-FP) and anti-NTD
279 non-supersite mAbs. In parallel, the group composed of anti-NTD supersite and all anti-RBDs
280 mAbs is less affected. These results align and expand our previous observations that Cv2.9116
281 binding to infected cells is more affected by TMPRSS2 than S309. Overall, mAbs of distinct
282 specificities are not equally sensitive to TMPRSS2 overexpression, with those targeting the S2
283 subunit being the most impacted.

284

285 *TMPRSS2 expression reduces antibody recognition of SARS-CoV-2 variants and other*
286 *members of the Coronaviridae family.*

287 We further aimed to evaluate the conservation of TMPRSS2-mediated decrease of S
288 recognition by mAbs across SARS-CoV-2 variants. We co-transfected TMPRSS2 and S
289 proteins from 10 different SARS-CoV-2 variants spanning the pandemic (from D614G to
290 KP.3.1.1) and evaluated Cv2.9116 binding **(Fig. 3A)**. The binding consistently decreases with
291 TMPRSS2 expression, independently of the viral variants **(Fig. 3B** and **S3A)**. Using the same
292 methodology, we investigate Cv2.9116 binding to different coronavirus S proteins including
293 human coronavirus 229E (alphacoronavirus) and SARS-CoV-2-related bat coronaviruses
294 (RaTG13 and BANAL 20-236). Of note, OC43 could not be included as its S protein is not
295 exported at the plasma membrane (Sadasivan et al., 2017). TMPRSS2 significantly lowers
296 Cv2.9116 binding to 229E and RaTG13 S, whereas binding to BANAL 20-236 S is not affected
297 in any condition **(Fig. 3C**, **Fig. S3B** and **S3C)**. Note that the low levels of NL63-S expression
298 impair accurate quantification, but we still observe that catalytically active TMPRSS2 reduces
299 the binding of Cv2.9116 **(Fig. S3C)**. These results show that the ability of TMPRSS2 to

300 promote the escape of S-expressing cells from anti-S2 antibodies is not restricted to SARS-
301 CoV-2.
302
303 *Several members of the TMPRSS family decrease antibody binding on SARS-CoV-2 S.*
304 Next, we evaluated the capacity of 8 proteases from the TMPRSS family to decrease
305 antibody recognition of SARS-CoV-2 S. For this, we transfected myc-conjugated TMPRSS
306 proteases into 293T-S-D614G cells and assessed Cv2.9116 binding **(Fig. S3D** and **S3E)**.
307 TMPRSS11A and 11B slightly increase Cv2.9116 binding to 293T-S-D614G in TMPRSS-
308 expressing cells as compared to bystander cells **(Fig. S3E).** All other TMPRSS proteases induce
309 significant reductions in Cv2.9116 binding to 293T-S-D614G **(Fig. 3D)**. Interestingly,
310 TMPRSS2 transfection reduces binding of Cv2.9116 on both transfected and bystander cells,
311 suggesting a *cis*- and *trans*-action on S for TMPRSS2. Altogether, this data shows that the
312 capacity to decrease antibody recognition of SARS-CoV-2 S is shared by distinct members of
313 the TMPRSS family.
314
315 *TMPRSS2 promotes S conformational rearrangements and increases S1 shedding.*
316 We sought to investigate the mechanism by which TMPRSS2 decreases mAbs binding
317 to 293T-S-D614G. To this aim, we employed mAbs targeting a linear epitope within the HR2
318 region of S2 (Cv2.3132; (Planchais et al., 2024)) and a quaternary epitopes of the RBD (2-43 ;
319 (Liu et al., 2020)) to determine whether S is impacted in either quantity or conformation,
320 respectively. As a control of TMPRSS2 activity we used Cv2.9116 **(Fig. 4A, 4B** and **4C)**. As
321 described above, overexpression of TMPRSS2 decreases Cv2.9116 staining by a median of
322 83,3%. In contrast, the binding of Cv2.3132 is reduced by only a median of 15%, demonstrating
323 that a change in overall S quantity cannot fully explain the observed decrease in Cv2.9116
324 binding. 2-43 is decreased by a median 49,1%, consistent with either shedding of S1, a major
325 conformational change of S, or both **(Fig.4A, 4B** and **4C)**. We then perform an ACE2 binding
326 assay using a soluble ACE2 ectodomain (**Fig. 4D**), which shows a reduction in the MFI upon
327 TMPRSS2 transfection from 4266 to 1622. Therefore, we measured soluble S1 in the
328 supernatant of 293T-S-D614G cells either overexpressing TMPRSS2 or not by ELISA **(Fig.**
329 **4E)**. Catalytically active TMPRSS2 increases the levels of soluble S1 by an average of 1.8-fold
330 over both empty control plasmid and TMPRSS2 S441A (**Fig. 4E**). These data indicate that
331 TMPRSS2 elicits S1 shedding. Note that we observe a similar shedding of S1 upon TMPRSS2
332 transfection with 293T-S-BA.5 (**Fig. S4A**, **B**, **C** and **D**). Taken together, these results
333 demonstrate that TMPRSS2 marginally affects S surface levels, but rather promotes

334 conformational changes characterized by S1 shedding and a decreased susceptibility to anti-S2
335 antibodies.
336
337 Considering that we and others have previously reported that TMPRSS2 increases S
338 fusogenicity (Bestle et al., 2020; Buchrieser et al., 2020), TMPRSS2-mediated S1 shedding and
339 lower ACE2 binding appears counter-intuitive. Therefore, we evaluated cell-cell fusion in the
340 same conditions in which we observed a decrease of mAbs binding by TMPRSS2, using an
341 acceptor-donor GFP-split assay (**Fig. 5A**). Regardless of whether TMPRSS2 is expressed by
342 donor, acceptor or both cells, it increases S fusogenicity with ACE2-expressing (**Fig. 5B**, **5C**,
343 and **S4E**). Interestingly, TMPRSS2 does not increase ACE2-independent fusion, which remains
344 comparable to background (**Fig. 5D, 5E**, and **S4E**), suggesting that the decrease in ACE2
345 binding is not compensated by an unspecific triggering of fusion. Similarly, TMPRSS2
346 increases only ACE2-dependent cell-cell fusion of 293T-S-BA.5 (**Fig. S4F** and **S4G**). Overall,
347 these results suggest that while TMPRSS2 reduces the number of S capable of binding ACE2,
348 the remaining S are more efficient at eliciting fusion upon ACE2 engagement.
349
350 *TMPRSS2 decreases serum-mediated ADCC of S-expressing cells*
351 Next, we sought to investigate whether TMPRSS2 expression decreases the binding of
352 polyclonal anti-S antibodies. We used immune sera from individuals with hybrid immunity (n
353 = 15; Wuhan infection, followed by 3 doses of mRNA vaccination; **Table 2**). Transfection of
354 TMPRSS2 reduces the binding of these sera to 293T-S-D614G by 52% (min 45,5 - max 56,3),
355 as measured by IgG staining (**Fig. 6A**). Similarly, treatment of Caco2-S-D614G with Camostat
356 increases the binding of polyclonal IgG and IgA antibodies (**Fig. S5A**). As expected, TMPRSS2
357 expression does not change the binding of pre-pandemic sera, which remained negative (**Fig.**
358 **S5B**). Infected Caco2 cells with D614G or XBB1.5 variants show a similar increase in serum
359 IgG binding to infected cells after 24h of Camostat treatment **(Fig. 6B** and **S5C)**. In IGROV-1
360 cells, overexpression of TMPRSS2 lowers IgG binding to cells infected with either D614G or
361 XBB1.5 **(Fig. 6C** and **S5D)**. This data indicates that endogenous levels of TMPRSS2 and/or
362 serine-proteases decrease the recognition of SARS-CoV-2 infected cells by antibodies present
363 in the sera of hybrid immune individuals.
364
365 To evaluate if lower binding of serum IgGs from individuals with hybrid immunity
366 translates into lower ADCC induction, we co-cultivate TMPRSS2-transfected 293T-S-D614G
367 with CD16-NFAT reporter Jurkat cells (**Fig. 6D**). We observe that TMPRSS2 transfection

368 significantly lowers CD16 activation median from 3,7 to 2,8, representing a median 30% (min
369 38,9% - max 46,5%) decrease (**Fig. 6E**). This highlights that the capacity of TMPRSS2 to lower
370 antibody binding results in impaired CD16 engagement and downstream signaling, which is an
371 accurate indicator of ADCC induction against infected cells (Dufloo et al., 2021).
372
373 *TMPRSS2 expression in infected cells marginally affects viral progeny*
374 Finally, we aim to determine whether TMPRSS2 expression in infected cells can impact
375 the antibody response to the viral progeny. For this, we produced two independent batches of
376 the D614G variant in IGROV-1 cells either expressing TMPRSS2 or not to analyze the released
377 viruses for infectivity and antibody sensitivity (**Fig. 7A**). We observed that TMPRSS2
378 expression in infected cells accounts for higher infectious titers at 2 days post-infection ($3{,}4.10^6$
379 vs 1.10^6), but the difference diminishes at 3 dpi (**Fig. 7B**), possibly because of an increased
380 cytopathic effect in TMPRSS2-expressing cells (not shown). Interestingly, viral genome copies
381 in the supernatant are not significantly different between cellular backgrounds. Thus, the ratio
382 of infectious genomes (RNA copies per infectious units) is slightly higher for viruses produced
383 in IGROV-1 TMPRSS2$^+$ at 2 dpi. These results indicate that TMPRSS2 presence in infected
384 cells renders viral progeny slightly more infectious at early time points.
385
386 We further employ flow virometry to evaluate antibody binding to viral particles
387 produced in each cellular background, using a selection of mAbs (SA55, S309, Cv2.9116,
388 Cv2.3132, Cv2.8145 and CoV44-62). We identify viral particles as events of around 80-90 nm
389 in size and positive for the nucleic acid dye Syto24 (**Fig. 7C**). We do not observe any difference
390 in mAb binding (**Fig. 7D** and **S6**), apart from SA55, which exhibits a modest decrease.
391 Altogether, these results suggest that TMPRSS2 expression in infected cells has only moderate
392 effects on S antigenicity in the viral progeny.
393
394

395 **Discussion**

396 Our study shows that TMPRSS2 makes the plasma membrane-associated S less sensitive
397 to recognition by antibodies and subsequent ADCC. We show that this activity requires a
398 catalytically active TMPRSS2. Its presence only marginally affects surface S level at the
399 membrane, indicating that TMPRSS2 does not reduces antibody binding because of a
400 degradation of S. We observe an increased S1 shedding, which likely explains the decrease in
401 binding of anti-S1 antibodies (i.e. anti-RBD and anti-NTD). Anti-S2 antibodies are more
402 affected by TMPRSS2-mediated evasion, a finding that cannot be explained by the shedding of
403 S1. Therefore, the S2 domain must adopt a conformation less susceptible to antibody binding.
404 Recent studies have identified an intermediate state of the S protein, characterized by partial
405 shedding and reversible rearrangement of S2 (Olmedillas et al., 2025). Combining our data
406 with these structural insights, we propose a model where TMPRSS2 destabilizes S through
407 cleavage, enabling S to adopt a conformation in-between pre- and post-fusion states, which is
408 less recognized by antibodies.

409

410 TMPRSS2 cleaves S at multiple sites (Fraser et al., 2022). We do not identify the
411 contribution of each of those sites to the phenotype. At least two of these cleavage sites seem
412 relevant to the phenomenon reported here. First, TMPRSS2 can cleave the Arg-Ser peptide
413 bond of the furin cleavage site (R–X–[K/R]–R↓–S) and therefore promotes shedding by
414 favoring S1 and S2 dissociation. Second, cleavage of the S2' site can account for the preferential
415 impact on anti-S2 antibodies by disrupting local epitopes required for anti-S2 binding, as many
416 FP epitopes overlap with the S2' site (Dacon et al., 2022; Low et al., 2022; Rosen et al., 2024).
417 It is also plausible that cleavage of S2' increases the overall flexibly of S2 (Olmedillas et al.,
418 2025), enabling this subunit to sample conformations that would hide key epitopes. Cleavage
419 of S2' can occur on the closed trimer independently of S1 shedding (Fraser et al., 2022), as the
420 Arg is not buried within the trimer, explaining why TMPRSS2 can reduce antibody binding to
421 S in the absence of ACE2. Our study clearly demonstrates the overall impact of TMPRSS2 on
422 S recognition by antibodies, but how each cleavage sites combine to affect overall S antigenicity
423 remains to be elucidated.

424

425 Our results also suggest that TMPRSS2 affects S present at the plasma membrane of
426 infected cells more than S proteins incorporated into viral particles. This finding aligns with
427 SARS-CoV-2 budding in the ERGIC compartment and exiting cells through a mixed
428 lysosomal-secretion pathway (Chen et al., 2021; Miura et al., 2023; Scherer et al., 2022). This

429 intracellular assembly of viral progeny most likely prevents contacts between virion-associated
430 S and activated TMPRSS2, which is preferentially located at the plasma membrane (Zhang et
431 al., 2022). Importantly, shedding of S at the plasma membrane may still interfere with the
432 neutralization of viral particles by generating soluble S1 decoy, as previously shown for SARS-
433 CoV-1 (Glowacka et al., 2011). A similar mechanism can operate in SARS-CoV-2 infected
434 cells.
435
436 As the physiological antibody response to SARS-CoV-2 infection and vaccination is
437 inherently polyclonal, we used immune positive sera from a hybrid immunity cohort.
438 TMPRSS2 decreases S binding and ADCC potency of these serum antibodies. Although the
439 CD16 reporter assay used differs from genuine ADCC assays, we have previously reported a
440 strong correlation between this assay and NK cell-mediated ADCC of SARS-CoV-2 infected
441 cells (Dufloo et al., 2021).
442
443 SARS-CoV-2 variants have evolved to escape anti-S binding and neutralization (Planas
444 et al., 2024, 2022, 2021; Uraki et al., 2026). Viral variants also differ in the proteolytic
445 processing of S, as the efficiency of the S1/S2 cleavage gradually increased while the usage of
446 TMPRSS2 decreased with Omicron emergence. TMPRSS2 decreases antibody binding against
447 all variants tested, indicating that it does not correlate with TMPRSS2 usage bias (Meng et al.,
448 2022). Differential TMPRSS2 impact on the anti-S2 pan-coronavirus Cv2.9116 binding across
449 the *Coronaviridae* family is also informative, as all coronaviruses share a conserved S2'
450 cleavage sequence, although the non-SARS-CoV-2 viruses tested here lack the FCS (Chan and
451 Zhan, 2021; Hoffmann et al., 2020; Temmam et al., 2022). As previous studies reported
452 multiple cleavage sites by TMPRSS2 in SARS-CoV and SARS-CoV-2 S (Fraser et al., 2022;
453 Glowacka et al., 2011), it is plausible that other cleavage sites may be involved, and possibly
454 differ across *Coronavidae*.
455
456 It is well established that anti-S2 Abs are cross-reactive, elicit effector functions, mediate
457 *in vivo* protection in animal models and protects against severe disease in clinical studies
458 (Dacon et al., 2022; Guenthoer et al., 2024; Ng et al., 2022, 2021; Stravalaci et al., 2022; Zhou
459 et al., 2023). Hence, lowering the binding of anti-S2 antibodies by TMPRSS2 could be a
460 mechanism by which SARS-CoV-2 escapes these cross-reactive antibodies.
461

We also show that other TMPRSS mediate Ab-escape. This aligns with previous reports indicating that TMPRSS4, 11D, 11E and 13 increase SARS-CoV-2 infection *in vitro* (Kishimoto et al., 2021; Zang et al., 2020). TMPRSS2 expression level in dissociated primary ciliated cells is similar to that observed in transfected 293T. However, inhibition of TMPRSS2 (as well as other TMPRSS proteases) with Camostat mesylate treatment showed no significant efficacy against COVID-19 in clinical trials (Khan et al., 2024). Given our results, it would be interesting to investigate the possible antiviral synergy between Camostat and antibodies, especially the ones targeting S2. Overall, future work will uncover how cellular proteases cooperate to modulate S conformation and antibody escape to reveal potential new therapeutic targets.

In conclusion, our results highlight the diverse effects of TMPRSS2 on the SARS-CoV-2 cycle and uncover a new mechanism by which cells infected by SARS-CoV-2 avoid the humoral immune response.

Acknowledgments

We thank members of the Virus and Immunity Unit for discussions and help in the preparation of this manuscript. We thank Jocelyne Creff and Fabienne Tzvetkov-Ricard for their technical and administrative assistance. We thank N. Aulner, N. Mahtal, J. Fernandes and the UtechS Photonic BioImaging core facility (Institut Pasteur). We thank Divya Unni and the Institut Pasteur grant office for their invaluable assistance in funding acquisition. We thank all the staff members of the Occupational Health and Medicine Department of the Hospices Civils de Lyon and staff members who contributed to the COVID-Ser clinical, all the clinical research associates for excellent work, and all the members of the clinical research and innovation department for reactivity (DRS, Hospices Civils de Lyon), in particular Pr Jean-Baptiste Fassier. Last, we thank all the patients and the health care workers for participation in this clinical study. Human biological samples and associated data were obtained from NeuroBioTec (CRB HCL, Lyon France, Biobank BB-0033-00046).

Fundings

This work is funded by Institut Pasteur, ANRS-MIE (D25266 IMMUNO-COVID), the Vaccine Research Institute (ANR-10-LABX-77), and the ANR young investigator program (ANR-23-CE15-0039-01 MACOVA). The funders had no role in the design or writing of the

article. UtechS Photonic BioImaging is funded by grant no. ANR-10-INSB-04-01, no. ANR-24- INBS- 0005 FBI (BIOGEN) and Région Ile-de-France programme DIM1-Health. This study received funding from the Agence Nationale de Recherches sur le Sida et les Hépatites Virales (ANRS-0154) and Fondation des Hospices Civils de Lyon for the COVID-Ser cohort. We acknowledge support from Institut Pasteur for the use of the Opera Phenix Plus microscope.

Author contributions

Experimental strategy and design: A.C.C., O.S. and T.B.

Laboratory experiments: A.C.C., A.D.C., C.P., F.P., M.K., M.J.G., E.T., A.W., I.S., F.G.B., P.R., I.F., J.B. and T.B.

Viral strains and key reagents and techniques: I.S., F.G.B., F.P., C.P., P.R. and H.M.

Cohort management and clinical research: S.T.A

Funding acquisition: O.S., H.M. and T.B.

Manuscript writing & editing: A.C.C, F.R., H.M., O.S and T.B

Conflict of interest

All authors declare no conflicts of interest.

Inclusion and diversity

We support inclusive, diverse, and equitable conduct of research.

References

Bean, D.J., Liang, Y.M., Avila, F., He, X., Asundi, A., Sagar, M., 2025. Endemic coronavirus infection is associated with SARS-CoV-2 Fc receptor-binding antibodies. J Virol e0055025. https://doi.org/10.1128/jvi.00550-25

Bestle, D., Heindl, M.R., Limburg, H., Van, T.V.L., Pilgram, O., Moulton, H., Stein, D.A., Hardes, K., Eickmann, M., Dolnik, O., Rohde, C., Klenk, H.-D., Garten, W., Steinmetzer, T., Böttcher-Friebertshäuser, E., 2020. TMPRSS2 and furin are both essential for proteolytic activation of SARS-CoV-2 in human airway cells. Life Science Alliance 3. https://doi.org/10.26508/lsa.202000786

Boson, B., Legros, V., Zhou, B., Siret, E., Mathieu, C., Cosset, F.-L., Lavillette, D., Denolly, S., 2021. The SARS-CoV-2 envelope and membrane proteins modulate maturation and retention of the spike protein, allowing assembly of virus-like particles. Journal of Biological Chemistry 296, 100111. https://doi.org/10.1074/jbc.RA120.016175

Buchrieser, J., Degrelle, S.A., Couderc, T., Nevers, Q., Disson, O., Manet, C., Donahue, D.A., Porrot, F., Hillion, K.-H., Perthame, E., Arroyo, M.V., Souquere, S., Ruigrok, K., Dupressoir, A., Heidmann, T., Montagutelli, X., Fournier, T., Lecuit, M., Schwartz, O., 2019. IFITM proteins inhibit placental syncytiotrophoblast formation and promote fetal demise. Science 365, 176–180. https://doi.org/10.1126/science.aaw7733

Buchrieser, J., Dufloo, J., Hubert, M., Monel, B., Planas, D., Rajah, M.M., Planchais, C., Porrot, F., Guivel-Benhassine, F., Van der Werf, S., Casartelli, N., Mouquet, H., Bruel, T., Schwartz, O., 2020. Syncytia formation by SARS-CoV-2-infected cells. The EMBO Journal 39, e106267. https://doi.org/10.15252/embj.2020106267

Cattin-Ortolá, J., Welch, L.G., Maslen, S.L., Papa, G., James, L.C., Munro, S., 2021. Sequences in the cytoplasmic tail of SARS-CoV-2 Spike facilitate expression at the cell surface and syncytia formation. Nat Commun 12, 5333. https://doi.org/10.1038/s41467-021-25589-1

Chan, Y.A., Zhan, S.H., 2021. The Emergence of the Spike Furin Cleavage Site in SARS-CoV-2. Mol Biol Evol 39, msab327. https://doi.org/10.1093/molbev/msab327

Chen, D., Zheng, Q., Sun, L., Ji, M., Li, Y., Deng, H., Zhang, H., 2021. ORF3a of SARS-CoV-2 promotes lysosomal exocytosis-mediated viral egress. Dev Cell 56, 3250-3263.e5. https://doi.org/10.1016/j.devcel.2021.10.006

Clark, J.J., Hoxie, I., Adelsberg, D.C., Sapse, I.A., Andreata-Santos, R., Yong, J.S., Amanat, F., Tcheou, J., Raskin, A., Singh, G., González-Domínguez, I., Edgar, J.E., Bournazos, S., Sun, W., Carreño, J.M., Simon, V., Ellebedy, A.H., Bajic, G., Krammer, F., 2024. Protective effect and molecular mechanisms of human non-neutralizing cross-reactive spike antibodies elicited by SARS-CoV-2 mRNA vaccination. Cell Reports 43, 114922. https://doi.org/10.1016/j.celrep.2024.114922

Dacon, C., Tucker, C., Peng, L., Lee, C.-C.D., Lin, T.-H., Yuan, M., Cong, Y., Wang, L., Purser, L., Williams, J.K., Pyo, C.-W., Kosik, I., Hu, Z., Zhao, M., Mohan, D., Cooper, A.J.R., Peterson, M., Skinner, J., Dixit, S., Kollins, E., Huzella, L., Perry, D., Byrum, R., Lembirik, S., Drawbaugh, D., Eaton, B., Zhang, Y., Yang, E.S., Chen, M., Leung, K., Weinberg, R.S., Pegu, A., Geraghty, D.E., Davidson, E., Douagi, I., Moir, S., Yewdell, J.W., Schmaljohn, C., Crompton, P.D., Holbrook, M.R., Nemazee, D., Mascola, J.R., Wilson, I.A., Tan, J., 2022. Broadly neutralizing antibodies target the

coronavirus fusion peptide. Science 377, 728–735. https://doi.org/10.1126/science.abq3773

Dey, D., Singh, S., Khan, S., Martin, M., Schnicker, N.J., Gakhar, L., Pierce, B.G., Hasan, S.S., 2022. An extended motif in the SARS-CoV-2 spike modulates binding and release of host coatomer in retrograde trafficking. Commun Biol 5, 1–13. https://doi.org/10.1038/s42003-022-03063-y

Dufloo, J., Grzelak, L., Staropoli, I., Madec, Y., Tondeur, L., Anna, F., Pelleau, S., Wiedemann, A., Planchais, C., Buchrieser, J., Robinot, R., Ungeheuer, M.-N., Mouquet, H., Charneau, P., White, M., Lévy, Y., Hoen, B., Fontanet, A., Schwartz, O., Bruel, T., 2021. Asymptomatic and symptomatic SARS-CoV-2 infections elicit polyfunctional antibodies. Cell Rep Med 2, 100275. https://doi.org/10.1016/j.xcrm.2021.100275

Earle, K.A., Ambrosino, D.M., Fiore-Gartland, A., Goldblatt, D., Gilbert, P.B., Siber, G.R., Dull, P., Plotkin, S.A., 2021. Evidence for antibody as a protective correlate for COVID-19 vaccines. Vaccine 39, 4423–4428. https://doi.org/10.1016/j.vaccine.2021.05.063

Fraser, B.J., Beldar, S., Seitova, A., Hutchinson, A., Mannar, D., Li, Y., Kwon, D., Tan, R., Wilson, R.P., Leopold, K., Subramaniam, S., Halabelian, L., Arrowsmith, C.H., Bénard, F., 2022. Structure and activity of human TMPRSS2 protease implicated in SARS-CoV-2 activation. Nat Chem Biol 18, 963–971. https://doi.org/10.1038/s41589-022-01059-7

Glowacka, I., Bertram, S., Müller, M.A., Allen, P., Soilleux, E., Pfefferle, S., Steffen, I., Tsegaye, T.S., He, Y., Gnirss, K., Niemeyer, D., Schneider, H., Drosten, C., Pöhlmann, S., 2011. Evidence that TMPRSS2 Activates the Severe Acute Respiratory Syndrome Coronavirus Spike Protein for Membrane Fusion and Reduces Viral Control by the Humoral Immune Response ▿ . J Virol 85, 4122–4134. https://doi.org/10.1128/JVI.02232-10

Goldblatt, D., Alter, G., Crotty, Sh., Plotkin, S., 2022. Correlates of Protection Against SARS CoV-2 Infection and Covid 19 Disease. https://doi.org/10.5281/zenodo.6375936

Grunst, M.W., Qin, Z., Dodero-Rojas, E., Ding, S., Prévost, J., Chen, Y., Hu, Y., Pazgier, M., Wu, S., Xie, X., Finzi, A., Onuchic, J.N., Whitford, P.C., Mothes, W., Li, W., 2024. Structure and inhibition of SARS-CoV-2 spike refolding in membranes. Science 385, 757–765. https://doi.org/10.1126/science.adn5658

Guenthoer, J., Garrett, M.E., Lilly, M., Depierreux, D.M., Ruiz, F., Chi, M., Stoddard, C.I., Chohan, V., Yaffe, Z.A., Sung, K., Ralph, D., Chu, H.Y., Iv, F.A.M., Overbaugh, J., 2024. The S2 subunit of spike encodes diverse targets for functional antibody responses to SARS-CoV-2. PLOS Pathogens 20, e1012383. https://doi.org/10.1371/journal.ppat.1012383

Hills, F.R., Geoghegan, J.L., Bostina, M., 2025. Architects of infection: A structural overview of SARS-related coronavirus spike glycoproteins. Virology 604, 110383. https://doi.org/10.1016/j.virol.2024.110383

Hoffmann, M., Hofmann-Winkler, H., Smith, J.C., Krüger, N., Arora, P., Sørensen, L.K., Søgaard, O.S., Hasselstrøm, J.B., Winkler, M., Hempel, T., Raich, L., Olsson, S., Danov, O., Jonigk, D., Yamazoe, T., Yamatsuta, K., Mizuno, H., Ludwig, S., Noé, F., Kjolby, M., Braun, A., Sheltzer, J.M., Pöhlmann, S., 2021. Camostat mesylate inhibits SARS-CoV-2 activation by TMPRSS2-related proteases and its metabolite

GBPA exerts antiviral activity. EBioMedicine 65, 103255. https://doi.org/10.1016/j.ebiom.2021.103255

Hoffmann, M., Kleine-Weber, H., Pöhlmann, S., 2020. A Multibasic Cleavage Site in the Spike Protein of SARS-CoV-2 Is Essential for Infection of Human Lung Cells. Molecular Cell 78, 779-784.e5. https://doi.org/10.1016/j.molcel.2020.04.022

Jian, F., Wang, J., Yisimayi, A., Song, W., Xu, Y., Chen, X., Niu, X., Yang, S., Yu, Y., Wang, P., Sun, H., Yu, L., Wang, J., Wang, Yao, An, R., Wang, W., Ma, M., Xiao, T., Gu, Q., Shao, F., Wang, Youchun, Shen, Z., Jin, R., Cao, Y., 2024. Evolving antibody response to SARS-CoV-2 antigenic shift from XBB to JN.1. Nature. https://doi.org/10.1038/s41586-024-08315-x

Ju, B., Zhang, Q., Ge, J., Wang, R., Sun, J., Ge, X., Yu, Jiazhen, Shan, S., Zhou, B., Song, S., Tang, X., Yu, Jinfang, Lan, J., Yuan, J., Wang, H., Zhao, Juanjuan, Zhang, S., Wang, Y., Shi, X., Liu, L., Zhao, Jincun, Wang, X., Zhang, Z., Zhang, L., 2020. Human neutralizing antibodies elicited by SARS-CoV-2 infection. Nature 1–5. https://doi.org/10.1038/s41586-020-2380-z

Kakizaki, M., Hashimoto, R., Nagata, N., Yamamoto, T., Okura, T., Katoh, H., Kitai, Y., Akahori, Y., Shirato, K., Ryo, A., Takayama, K., Takeda, M., 2024. The respective roles of TMPRSS2 and cathepsins for SARS-CoV-2 infection in human respiratory organoids. J Virol e0185324. https://doi.org/10.1128/jvi.01853-24

Khan, U., Mubariz, M., Khlidj, Y., Nasir, M.M., Ramadan, S., Saeed, F., Muhammad, A., Abuelazm, M., 2024. Safety and Efficacy of Camostat Mesylate for Covid-19: a systematic review and Meta-analysis of Randomized controlled trials. BMC Infectious Diseases 24, 709. https://doi.org/10.1186/s12879-024-09468-w

Khoury, D.S., Cromer, D., Reynaldi, A., Schlub, T.E., Wheatley, A.K., Juno, J.A., Subbarao, K., Kent, S.J., Triccas, J.A., Davenport, M.P., 2021. Neutralizing antibody levels are highly predictive of immune protection from symptomatic SARS-CoV-2 infection. Nat Med 27, 1205–1211. https://doi.org/10.1038/s41591-021-01377-8

Kim, I.-J., Lee, Y.-H., Khalid, M.M., Chen, I.P., Zhang, Y., Ott, M., Verdin, E., 2023. SARS-CoV-2 protein ORF8 limits expression levels of Spike antigen and facilitates immune evasion of infected host cells. J Biol Chem 299, 104955. https://doi.org/10.1016/j.jbc.2023.104955

Kishimoto, M., Uemura, K., Sanaki, T., Sato, A., Hall, W.W., Kariwa, H., Orba, Y., Sawa, H., Sasaki, M., 2021. TMPRSS11D and TMPRSS13 Activate the SARS-CoV-2 Spike Protein. Viruses 13, 384. https://doi.org/10.3390/v13030384

Liu, L., Wang, P., Nair, M.S., Yu, J., Rapp, M., Wang, Q., Luo, Y., Chan, J.F.-W., Sahi, V., Figueroa, A., Guo, X.V., Cerutti, G., Bimela, J., Gorman, J., Zhou, T., Chen, Z., Yuen, K.-Y., Kwong, P.D., Sodroski, J.G., Yin, M.T., Sheng, Z., Huang, Y., Shapiro, L., Ho, D.D., 2020. Potent neutralizing antibodies against multiple epitopes on SARS-CoV-2 spike. Nature 584, 450–456. https://doi.org/10.1038/s41586-020-2571-7

Low, J.S., Jerak, J., Tortorici, M.A., McCallum, M., Pinto, D., Cassotta, A., Foglierini, M., Mele, F., Abdelnabi, R., Weynand, B., Noack, J., Montiel-Ruiz, M., Bianchi, S., Benigni, F., Sprugasci, N., Joshi, A., Bowen, J.E., Stewart, C., Rexhepaj, M., Walls, A.C., Jarrossay, D., Morone, D., Paparoditis, P., Garzoni, C., Ferrari, P., Ceschi, A., Neyts, J., Purcell, L.A., Snell, G., Corti, D., Lanzavecchia, A., Veesler, D., Sallusto, F., 2022. ACE2-binding exposes the SARS-CoV-2 fusion peptide to broadly neutralizing coronavirus antibodies. Science 377, 735–742. https://doi.org/10.1126/science.abq2679

Lu, X., Wang, L., Sakthivel, S.K., Whitaker, B., Murray, J., Kamili, S., Lynch, B., Malapati, L., Burke, S.A., Harcourt, J., Tamin, A., Thornburg, N.J., Villanueva, J.M., Lindstrom, S., 2020. US CDC Real-Time Reverse Transcription PCR Panel for Detection of Severe Acute Respiratory Syndrome Coronavirus 2. Emerg Infect Dis 26, 1654–1665. https://doi.org/10.3201/eid2608.201246

Lusvarghi, S., Vassell, R., Williams, B., Baha, H., Neerukonda, S.N., Weiss, C.D., 2025. Capture of fusion-intermediate conformations of SARS-CoV-2 spike requires receptor binding and cleavage at either the S1/S2 or S2' site. PLOS Pathogens 21, e1012808. https://doi.org/10.1371/journal.ppat.1012808

Marcink, T.C., Kicmal, T., Armbruster, E., Zhang, Z., Zipursky, G., Golub, K.L., Idris, M., Khao, J., Drew-Bear, J., McGill, G., Gallagher, T., Porotto, M., des Georges, A., Moscona, A., 2022. Intermediates in SARS-CoV-2 spike–mediated cell entry. Science Advances 8, eabo3153. https://doi.org/10.1126/sciadv.abo3153

Meng, B., Abdullahi, A., Ferreira, I.A.T.M., Goonawardane, N., Saito, A., Kimura, I., Yamasoba, D., Gerber, P.P., Fatihi, S., Rathore, S., Zepeda, S.K., Papa, G., Kemp, S.A., Ikeda, T., Toyoda, M., Tan, T.S., Kuramochi, J., Mitsunaga, S., Ueno, T., Shirakawa, K., Takaori-Kondo, A., Brevini, T., Mallery, D.L., Charles, O.J., Bowen, J.E., Joshi, A., Walls, A.C., Jackson, L., Martin, D., Smith, K.G.C., Bradley, J., Briggs, J.A.G., Choi, J., Madissoon, E., Meyer, K.B., Mlcochova, P., Ceron-Gutierrez, L., Doffinger, R., Teichmann, S.A., Fisher, A.J., Pizzuto, M.S., de Marco, A., Corti, D., Hosmillo, M., Lee, J.H., James, L.C., Thukral, L., Veesler, D., Sigal, A., Sampaziotis, F., Goodfellow, I.G., Matheson, N.J., Sato, K., Gupta, R.K., 2022. Altered TMPRSS2 usage by SARS-CoV-2 Omicron impacts infectivity and fusogenicity. Nature 603, 706–714. https://doi.org/10.1038/s41586-022-04474-x

Miura, K., Suzuki, Y., Ishida, K., Arakawa, M., Wu, H., Fujioka, Y., Emi, A., Maeda, K., Hamajima, R., Nakano, T., Tenno, T., Hiroaki, H., Morita, E., 2023. Distinct motifs in the E protein are required for SARS-CoV-2 virus particle formation and lysosomal deacidification in host cells. Journal of Virology 97, e00426-23. https://doi.org/10.1128/jvi.00426-23

Natarajan, H., Crowley, A.R., Butler, S.E., Xu, S., Weiner, J.A., Bloch, E.M., Littlefield, K., Wieland-Alter, W., Connor, R.I., Wright, P.F., Benner, S.E., Bonny, T.S., Laeyendecker, O., Sullivan, D., Shoham, S., Quinn, T.C., Larman, H.B., Casadevall, A., Pekosz, A., Redd, A.D., Tobian, A.A.R., Ackerman, M.E., 2021. Markers of Polyfunctional SARS-CoV-2 Antibodies in Convalescent Plasma. mBio 12, e00765-21. https://doi.org/10.1128/mBio.00765-21

Ng, K.W., Faulkner, N., Finsterbusch, K., Wu, M., Harvey, R., Hussain, S., Greco, M., Liu, Y., Kjaer, S., Swanton, C., Gandhi, S., Beale, R., Gamblin, S.J., Cherepanov, P., McCauley, J., Daniels, R., Howell, M., Arase, H., Wack, A., Bauer, D.L.V., Kassiotis, G., 2022. SARS-CoV-2 S2–targeted vaccination elicits broadly neutralizing antibodies. Science Translational Medicine 14, eabn3715. https://doi.org/10.1126/scitranslmed.abn3715

Ng, K.W., Faulkner, N., Wrobel, A.G., Gamblin, S.J., Kassiotis, G., 2021. Heterologous humoral immunity to human and zoonotic coronaviruses: Aiming for the achilles heel. Semin Immunol 55, 101507. https://doi.org/10.1016/j.smim.2021.101507

Olmedillas, E., Rajamanickam, R.R., Avalos, R.D., Ana-Sosa-Batiz, F., Zyla, D., Zandonatti, M.A., Harkins, S.S., Shresta, S., Hastie, K.M., Saphire, E.O., 2025.

Structure of a SARS-CoV-2 spike S2 subunit in a pre-fusion, open conformation. Cell Reports 44, 116052. https://doi.org/10.1016/j.celrep.2025.116052

Pinto, D., Park, Y.-J., Beltramello, M., Walls, A.C., Tortorici, M.A., Bianchi, S., Jaconi, S., Culap, K., Zatta, F., De Marco, A., Peter, A., Guarino, B., Spreafico, R., Cameroni, E., Case, J.B., Chen, R.E., Havenar-Daughton, C., Snell, G., Telenti, A., Virgin, H.W., Lanzavecchia, A., Diamond, M.S., Fink, K., Veesler, D., Corti, D., 2020. Cross-neutralization of SARS-CoV-2 by a human monoclonal SARS-CoV antibody. Nature 583, 290–295. https://doi.org/10.1038/s41586-020-2349-y

Planas, D., Saunders, N., Maes, P., Guivel-Benhassine, F., Planchais, C., Buchrieser, J., Bolland, W.-H., Porrot, F., Staropoli, I., Lemoine, F., Péré, H., Veyer, D., Puech, J., Rodary, J., Baele, G., Dellicour, S., Raymenants, J., Gorissen, S., Geenen, C., Vanmechelen, B., Wawina-Bokalanga, T., Martí-Carreras, J., Cuypers, L., Sève, A., Hocqueloux, L., Prazuck, T., Rey, F.A., Simon-Loriere, E., Bruel, T., Mouquet, H., André, E., Schwartz, O., 2022. Considerable escape of SARS-CoV-2 Omicron to antibody neutralization. Nature 602, 671–675. https://doi.org/10.1038/s41586-021-04389-z

Planas, D., Staropoli, I., Michel, V., Lemoine, F., Donati, F., Prot, M., Porrot, F., Guivel-Benhassine, F., Jeyarajah, B., Brisebarre, A., Dehan, O., Avon, L., Bolland, W.H., Hubert, M., Buchrieser, J., Vanhoucke, T., Rosenbaum, P., Veyer, D., Péré, H., Lina, B., Trouillet-Assant, S., Hocqueloux, L., Prazuck, T., Simon-Loriere, E., Schwartz, O., 2024. Distinct evolution of SARS-CoV-2 Omicron XBB and BA.2.86/JN.1 lineages combining increased fitness and antibody evasion. Nat Commun 15, 2254. https://doi.org/10.1038/s41467-024-46490-7

Planas, D., Veyer, D., Baidaliuk, A., Staropoli, I., Guivel-Benhassine, F., Rajah, M.M., Planchais, C., Porrot, F., Robillard, N., Puech, J., Prot, M., Gallais, F., Gantner, P., Velay, A., Le Guen, J., Kassis-Chikhani, N., Edriss, D., Belec, L., Seve, A., Courtellemont, L., Péré, H., Hocqueloux, L., Fafi-Kremer, S., Prazuck, T., Mouquet, H., Bruel, T., Simon-Lorière, E., Rey, F.A., Schwartz, O., 2021. Reduced sensitivity of SARS-CoV-2 variant Delta to antibody neutralization. Nature 596, 276–280. https://doi.org/10.1038/s41586-021-03777-9

Planchais, C., Fernández, I., Bruel, T., de Melo, G.D., Prot, M., Beretta, M., Guardado-Calvo, P., Dufloo, J., Molinos-Albert, L.M., Backovic, M., Chiaravalli, J., Giraud, E., Vesin, B., Conquet, L., Grzelak, L., Planas, D., Staropoli, I., Guivel-Benhassine, F., Hieu, T., Boullé, M., Cervantes-Gonzalez, M., Ungeheuer, M.-N., Charneau, P., van der Werf, S., Agou, F., French COVID Cohort Study Group, CORSER Study Group, Dimitrov, J.D., Simon-Lorière, E., Bourhy, H., Montagutelli, X., Rey, F.A., Schwartz, O., Mouquet, H., 2022. Potent human broadly SARS-CoV-2–neutralizing IgA and IgG antibodies effective against Omicron BA.1 and BA.2. Journal of Experimental Medicine 219, e20220638. https://doi.org/10.1084/jem.20220638

Planchais, C., Fernández, I., Chalopin, B., Bruel, T., Rosenbaum, P., Beretta, M., Dimitrov, J.D., Conquet, L., Donati, F., Prot, M., Porrot, F., Planas, D., Staropoli, I., Guivel-Benhassine, F., Baquero, E., van der Werf, S., Haouz, A., Simon-Lorière, E., Montagutelli, X., Maillère, B., Rey, F.A., Guardado-Calvo, P., Nozach, H., Schwartz, O., Mouquet, H., 2024. Broad sarbecovirus neutralization by combined memory B cell antibodies to ancestral SARS-CoV-2. iScience 27, 110354. https://doi.org/10.1016/j.isci.2024.110354

Rosen, L.E., Tortorici, M.A., De Marco, A., Pinto, D., Foreman, W.B., Taylor, A.L., Park, Y.-J., Bohan, D., Rietz, T., Errico, J.M., Hauser, K., Dang, H.V., Chartron, J.W., Giurdanella, M., Cusumano, G., Saliba, C., Zatta, F., Sprouse, K.R., Addetia, A., Zepeda, S.K., Brown, J., Lee, J., Dellota, E., Rajesh, A., Noack, J., Tao, Q., DaCosta, Y., Tsu, B., Acosta, R., Subramanian, S., de Melo, G.D., Kergoat, L., Zhang, I., Liu, Z., Guarino, B., Schmid, M.A., Schnell, G., Miller, J.L., Lempp, F.A., Czudnochowski, N., Cameroni, E., Whelan, S.P.J., Bourhy, H., Purcell, L.A., Benigni, F., di Iulio, J., Pizzuto, M.S., Lanzavecchia, A., Telenti, A., Snell, G., Corti, D., Veesler, D., Starr, T.N., 2024. A potent pan-sarbecovirus neutralizing antibody resilient to epitope diversification. Cell. https://doi.org/10.1016/j.cell.2024.09.026

Sadasivan, J., Singh, M., Sarma, J.D., 2017. Cytoplasmic tail of coronavirus spike protein has intracellular targeting signals. J Biosci 42, 231–244. https://doi.org/10.1007/s12038-017-9676-7

Saunders, N., Fernandez, I., Planchais, C., Michel, V., Rajah, M.M., Baquero Salazar, E., Postal, J., Porrot, F., Guivel-Benhassine, F., Blanc, C., Chauveau-Le Friec, G., Martin, A., Grzelak, L., Oktavia, R.M., Meola, A., Ahouzi, O., Hoover-Watson, H., Prot, M., Delaune, D., Cornelissen, M., Deijs, M., Meriaux, V., Mouquet, H., Simon-Lorière, E., van der Hoek, L., Lafaye, P., Rey, F., Buchrieser, J., Schwartz, O., 2023. TMPRSS2 is a functional receptor for human coronavirus HKU1. Nature 624, 207–214. https://doi.org/10.1038/s41586-023-06761-7

Scherer, K.M., Mascheroni, L., Carnell, G.W., Wunderlich, L.C.S., Makarchuk, S., Brockhoff, M., Mela, I., Fernandez-Villegas, A., Barysevich, M., Stewart, H., Suau Sans, M., George, C.L., Lamb, J.R., Kaminski-Schierle, G.S., Heeney, J.L., Kaminski, C.F., 2022. SARS-CoV-2 nucleocapsid protein adheres to replication organelles before viral assembly at the Golgi/ERGIC and lysosome-mediated egress. Science Advances 8, eabl4895. https://doi.org/10.1126/sciadv.abl4895

Sterlin, D., Mathian, A., Miyara, M., Mohr, A., Anna, F., Claër, L., Quentric, P., Fadlallah, J., Devilliers, H., Ghillani, P., Gunn, C., Hockett, R., Mudumba, S., Guihot, A., Luyt, C.-E., Mayaux, J., Beurton, A., Fourati, S., Bruel, T., Schwartz, O., Lacorte, J.-M., Yssel, H., Parizot, C., Dorgham, K., Charneau, P., Amoura, Z., Gorochov, G., 2021. IgA dominates the early neutralizing antibody response to SARS-CoV-2. Sci Transl Med 13, eabd2223. https://doi.org/10.1126/scitranslmed.abd2223

Stravalaci, M., Pagani, I., Paraboschi, E.M., Pedotti, M., Doni, A., Scavello, F., Mapelli, S.N., Sironi, M., Perucchini, C., Varani, L., Matkovic, M., Cavalli, A., Cesana, D., Gallina, P., Pedemonte, N., Capurro, V., Clementi, N., Mancini, N., Invernizzi, P., Bayarri-Olmos, R., Garred, P., Rappuoli, R., Duga, S., Bottazzi, B., Uguccioni, M., Asselta, R., Vicenzi, E., Mantovani, A., Garlanda, C., 2022. Recognition and inhibition of SARS-CoV-2 by humoral innate immunity pattern recognition molecules. Nat Immunol 23, 275–286. https://doi.org/10.1038/s41590-021-01114-w

Sztain, T., Ahn, S.-H., Bogetti, A.T., Casalino, L., Goldsmith, J.A., Seitz, E., McCool, R.S., Kearns, F.L., Acosta-Reyes, F., Maji, S., Mashayekhi, G., McCammon, J.A., Ourmazd, A., Frank, J., McLellan, J.S., Chong, L.T., Amaro, R.E., 2021. A glycan gate controls opening of the SARS-CoV-2 spike protein. Nat. Chem. 13, 963–968. https://doi.org/10.1038/s41557-021-00758-3

Temmam, S., Vongphayloth, K., Baquero, E., Munier, S., Bonomi, M., Regnault, B., Douangboubpha, B., Karami, Y., Chrétien, D., Sanamxay, D., Xayaphet, V., Paphaphanh, P., Lacoste, V., Somlor, S., Lakeomany, K., Phommavanh, N., Pérot, P., Dehan, O., Amara, F., Donati, F., Bigot, T., Nilges, M., Rey, F.A., van der Werf, S., Brey, P.T., Eloit, M., 2022. Bat coronaviruses related to SARS-CoV-2 and infectious for human cells. Nature 604, 330–336. https://doi.org/10.1038/s41586-022-04532-4

Uraki, R., Korber, B., Diamond, M.S., Kawaoka, Y., 2026. SARS-CoV-2 variants: biology, pathogenicity, immunity and control. Nat Rev Microbiol 24, 8–28. https://doi.org/10.1038/s41579-025-01255-x

Zang, R., Castro, M.F.G., McCune, B.T., Zeng, Q., Rothlauf, P.W., Sonnek, N.M., Liu, Z., Brulois, K.F., Wang, X., Greenberg, H.B., Diamond, M.S., Ciorba, M.A., Whelan, S.P.J., Ding, S., 2020. TMPRSS2 and TMPRSS4 promote SARS-CoV-2 infection of human small intestinal enterocytes. Science Immunology 5, eabc3582. https://doi.org/10.1126/sciimmunol.abc3582

Zhang, Q., Rosa, R.S.L., Ray, A., Durlet, K., Dorrazehi, G.M., Bernardi, R.C., Alsteens, D., 2025. Probing SARS-CoV-2 membrane binding peptide via single-molecule AFM-based force spectroscopy. Nat Commun 16, 6. https://doi.org/10.1038/s41467-024-55358-9

Zhang, Y., Sun, S., Du, C., Hu, K., Zhang, C., Liu, M., Wu, Q., Dong, N., 2022. Transmembrane serine protease TMPRSS2 implicated in SARS-CoV-2 infection is autoactivated intracellularly and requires N-glycosylation for regulation. Journal of Biological Chemistry 298, 102643. https://doi.org/10.1016/j.jbc.2022.102643

Zhou, P., Song, G., Liu, H., Yuan, M., He, W.-T., Beutler, N., Zhu, X., Tse, L.V., Martinez, D.R., Schäfer, A., Anzanello, F., Yong, P., Peng, L., Dueker, K., Musharrafieh, R., Callaghan, S., Capozzola, T., Limbo, O., Parren, M., Garcia, E., Rawlings, S.A., Smith, D.M., Nemazee, D., Jardine, J.G., Safonova, Y., Briney, B., Rogers, T.F., Wilson, I.A., Baric, R.S., Gralinski, L.E., Burton, D.R., Andrabi, R., 2023. Broadly neutralizing anti-S2 antibodies protect against all three human betacoronaviruses that cause deadly disease. Immunity 56, 669-686.e7. https://doi.org/10.1016/j.immuni.2023.02.005

Zost, S.J., Gilchuk, P., Chen, R.E., Case, J.B., Reidy, J.X., Trivette, A., Nargi, R.S., Sutton, R.E., Suryadevara, N., Chen, E.C., Binshtein, E., Shrihari, S., Ostrowski, M., Chu, H.Y., Didier, J.E., MacRenaris, K.W., Jones, T., Day, S., Myers, L., Eun-Hyung Lee, F., Nguyen, D.C., Sanz, I., Martinez, D.R., Rothlauf, P.W., Bloyet, L.-M., Whelan, S.P.J., Baric, R.S., Thackray, L.B., Diamond, M.S., Carnahan, R.H., Crowe, J.E., 2020. Rapid isolation and profiling of a diverse panel of human monoclonal antibodies targeting the SARS-CoV-2 spike protein. Nat Med 26, 1422–1427. https://doi.org/10.1038/s41591-020-0998-x

Figures Legend

Figure 1. TMPRSS2 decreases mAbs binding to cell surface Spike.

843 **(A)** Experimental procedure. 293T-S-D614G were transfected with TMPRSS2-mScarlet-I
844 plasmid overnight before surface staining with either Cv2.9116 or S309. **(B)** Representative
845 histogram of anti-S binding for each condition. Grey line represents MGO53 (isotype) control
846 for each transfection condition (colored) for Cv2.9116 and S309. **(C)** Raw MFI and %reduction
847 in S binding for Cv2.9116 and S309 for each transfection condition. Median of >3 independent
848 experiments are represented with 95% Confidence Intervals (CIs). **(D)** Experimental procedure
849 for Caco2 cells infection and representative dot plots of anti-S IgG quantification in NCP
850 positive cells (out of 3 independent experiments). **(E)** Experimental procedure for IGROV-1
851 cells infection and representative dot plots of anti-S IgG quantification in NCP positive cells
852 (out of 3 independent experiments).
853
854 **Figure 2. TMPRSS2-mediated decrease in mAb binding varies across Spike epitopes.**
855 **(A)** Raw MFI of each mAb and subsequent reduction in binding after TMPRSS2 transfection
856 in 293T-S-D614G are clustered by epitope specificity. Each column is a mAb and each square
857 represents the median value from at least 3 independent experiments. **(B)** Raw MFI and **(C)**
858 reduction in binding to 293T-S-D614G are represented by mAb class and epitope. **(D)**
859 Correlation between the reduction in binding upon TMPRSS2 expression and MFI of binding
860 in the absence of TMPRSS2 for each mAb. A spearman regression was performed.
861
862 **Figure 3. TMPRSS2 reduction of antibody binding is conserved across betacoronaviruses**
863 **and observed with other TMPRSS2-related proteases.**
864 **(A)** Experimental procedure. **(B)** Reduction in binding to SARS-CoV-2 S-positive cells upon
865 TMPRSS2 expression as compared to pEmpty using S from different SARS-CoV-2 variants.
866 **(C)** Reduction in binding to S-positive cells upon TMPRSS2 as compared to pEmpty using S
867 plasmids of different betacoronaviruses. **(D)** Reduction in binding of Cv2.9116 to 293T-S-
868 D614G transfected with different TMPRSS. Median with 95% CI are represented and each
869 point represents a single biological replicate. Statistical analyses were performed using two-
870 sided ANOVA, $p<0.05$ = *, $p<0.01$ = **, $p<0.001$ = ***, $p<0.0001$ = ****.
871
872 **Figure 4. TMPRSS2 effect on antibody binding is mediated by conformational changes of**
873 **Spike**
874 **(A)** Dot plot of Cv2.9116, Cv2.3132 and 2-43 binding to 293T-empty or 293T-S-D614G upon
875 transfection of pEmpty or TMPRSS2 WT. **(B)** Quantification of Cv2.3132, 2-43 and Cv2.9116
876 binding to 293T-S-D614G after TMPRSS2 transfection and **(C)** corresponding reduction in

877 binding. Mann-Whitney analysis was performed, $p<0.05$ = * for MFI and reduction in MFI was
878 analyzed using two-sided ANOVA, $p<0.0001$ = ****. **(D)** Soluble ACE2 MFI to 293T-S-
879 D614G. **(E)** Normalized Area Under the Curve (AUC) quantified by S1 ELISA in supernatants
880 after overnight transfection in 293T-S-D614G. Each point is a biological replicate and median
881 and 95% CI are represented. Mann-Whitney analysis was performed, $p<0.05$ = *.
882
883 **Figure 5. Evaluation of TMPRSS2 on S-mediated syncytia formation**
884 **(A)** Experimental design. **(B)** Representative images of spike-mediated fusion with $ACE2^+$
885 overexpressing 293T after TMPRSS2 transfection and **(C)** corresponding quantification.
886 Statistical analysis was performed using multiple Mann-Whitney tests, $p<0.05$ = *, $p<0.01$ =
887 **. **(D)** Representative images of spike-mediated fusion with WT overexpressing 293T after
888 TMPRSS2 transfection and **(E)** corresponding quantification. Shown are median and 95% CI
889 of all experiments while each point represents individual values from biological replicates.
890
891 **Figure 6. Seropositive serum binding evaluation in TMPRSS2 context.**
892 **(A)** Reduction of anti-S Abs binding from serum of individuals with hybrid immunity to 293T-
893 S-D614G expressing or not TMPRSS2 **(B)** Percentage of IgG bound to D61G4- or XBB1.5-
894 infected Caco2 cells by anti-S from the same sera after overnight treatment with camostat. **(C)**
895 Percentage of IgG bound to D61G4 or XBB1.5 infected IGROV-1 cells expressing or not
896 TMPRSS2 by the same sera. **(D)** Experimental procedure for CD16 reporter coculture assay
897 and **(E)** corresponding quantification of CD16 activation. Displayed are the median and 95%
898 confidence interval. Points represent individual values from biological replicates. Wilcoxon
899 statistical analysis was performed, $p<0.05$ = *, $p<0.0001$ = ****
900
901 **Figure 7. Evaluation of TMPRSS2 status in infected cells on the viral progeny.**
902 **(A)** Schematic outline of the procedure. **(B)** S-Fuse titration, nucleocaspid RT-qPCR and
903 Infectious genomes of supernatant from two independently produced stocks of D614G viruses,
904 measured in duplicates. **(C)** Flow virometry gating strategy to analyze anti-S binding to viral
905 population from WT IGROV-1 cells. **(D)** Representative histograms of binding intensity. WT
906 and TMPRSS2 conditions are represented in green and blue, respectively.
907
908 **Figure Suppl 1. TMPRSS2 catalytic activity confers lower anti-S binding.**
909 **(A)** Dot plots of the effect of simultaneous transfection with TMPRSS2 and Camostat treatment
910 of 293T-S-D614G on Cv2.3132, Cv2.9116 and S309 binding. Representative of three

911 biological replicates. **(B)** MFI of anti-MHC-I W6/32 binding to 293T-S-D614G transfected
912 either with pTMPRSS2 S441A or WT. Each point is a biological replicate, median and 95% CI
913 are represented. **(C)** Dot plots of the effect of overnight Camostat treatment of Caco2-S-D614G
914 Cv2.9116 and S309 binding. Representative of three biological replicates. **(D)** Gating strategy
915 for the analysis of Cv2.9116 and S309 binding to infected Caco2, represented for non-treated
916 Caco2 infected with D614G. **(E)** Dot plots of the effect of overnight Camostat treatment at 1dpi
917 XBB1.5 infected Caco2 on Cv2.9116 and S309 binding. Representative of three biological
918 replicates. **(F)** Gating strategy for the analysis of Cv2.9116 and S309 binding to infected
919 IGROV-1, represented for IGROV-1 WT infected with D614G. **(G)** Dot plots of the effect
920 TMPRSS2 in XBB1.5-infected Caco2 on Cv2.9116 and S309 binding representative of three
921 biological replicates. **(H)** Binding of anti-TMPRSS2 nanobody binding to different cells in a
922 representative histogram (left) where grey lines represent the MGO53 staining and the
923 corresponding plot (left).
924
925 **Figure Suppl 2. Extension of epitope screening of TMPRSS2-mediated decrease in mAb**
926 **binding to 293T-S-BA.5**
927 Raw MFI of each mAb and subsequent reduction in binding after TMPRSS2 transfection in
928 293T-S-BA.5 are clustered by epitope specificity. Antibodies showing baseline binding to
929 293T-S-BA.5 under 3 times the value of MGO53 (irrelevant mAb) were not considered for
930 reduction analysis and showed in grey. Each column is a mAb and each square represents the
931 median value from >3 independent experiments.
932
933 **Figure Suppl 3. Evaluation of TMPRSS activity on Cv2.9116 binding to different**
934 **coronaviruses spike.**
935 **(A** and **B)** Raw MFI of Cv2.9116 binding in co-transfected 293T cells. Dashed line represents
936 mean MGO53 MFI, as background measurement. MFI signal was analyzed using two-sided
937 ANOVA, $p<0.05$ = *, $p<0.01$ = **, $p<0.001$ = ***, $p<0.0001$ = ****. **(C)** Representative dot
938 plots of co-transfected 293T cells with different betacoronaviruses' S. **(D)** Representative dot
939 plots of Cv2.9116 binding to 293T-S-D614G cells transfected with different TMPRSS and **(E)**
940 Raw MFI. Each point is a biological replicate, median and 95% CI are represented. Dashed line
941 represents mean MGO53 MFI, as background measurement. MFI signal was analyzed using
942 two-sided ANOVA, $p<0.05$ = *, $p<0.01$ = **, $p<0.001$ = ***, $p<0.0001$ = ****.
943

944 **Figure Suppl 4. Extension of the mechanistic analysis of TMRPSS2 effect on mAb binding**
945 **on S-BA.5 and fusion.**
946 **(A)** Quantification of Cv2.3132, IgG 2-43 and Cv2.9116 binding to 293T-S-BA.5 after
947 TMPRSS2 transfection and **(B)** corresponding reduction in binding. Mann-Whitney analysis
948 was performed, $p<0.05$ = * for MFI while reduction in MFI was analyzed using two-sided
949 ANOVA, $p<0.0001$ = ****. **(C)** Soluble ACE2 MFI to 293T-S-BA.5. Histograms represent the
950 median and 95% CI of all experiments while each point represents individual values form
951 biological replicates. **(D)** Normalized area under the curve (AUC) quantified by S1 ELISA
952 contained in supernatants after overnight transfection in 293T-S-BA.5. Mann-Whitney analysis
953 was performed, $p<0.05$ = *. **(E** and **F)** Raw values of GFP area in μm^2 for ACE2-dependent
954 and ACE2-independent S-D614G- and S-BA.5 respectively mediated fusion after TMPRSS2
955 transfection in donor or acceptor cells. **(G)** GFP area normalized over non-transfected GFP area
956 for S-BA.5 donor cells upon TMPRSS2 transfection. Shown are the median of all experiments
957 and 95% CI with each point representing individual values form biological replicates. Statistical
958 analysis was performed using two-way ANOVA, $p<0.01$ = **.
959
960 **Figure Suppl 5. Analysis of serum Abs binding to membrane-bound spike.**
961 **(A)** Percentages of IgG and IgA positive Caco2-S-D614G upon overnight Camostat treatment.
962 Each point represents the mean of two independent measurements for each donor. Statistical
963 analysis was performed using two-sided ANOVA, $p<0.0001$ = ****. (**B**) Raw MFI of pre-
964 pandemic and seropositive sera to 293T-S-D614G transfected with TMPRSS2 or not. Each
965 point represents mean of three independent measurements for each donor. **(C)** Gating strategy
966 for evaluation of anti-S binding from sera binding gated on nucleocapsid-positive Caco2 cells,
967 exemplified for non-treated D614G-infected cells. (**D**) Gating strategy for evaluation of anti-S
968 binding from sera gated in nucleocapsid-positive IGROV-1, exemplified for WT D614G-
969 infected cells.
970
971 **Figure Suppl 6. Quantification of each mAb binding D614G produced in TMPRSS2**
972 **IGROV1 cells.** Each point is an independent measurement. Dashed line represents the minimal
973 and maximal MGO53 MFI obtained across the independent experiment. Each viral production
974 has been analyzed at least 2 times. Statistical analysis was performed using 2-sided ANOVA
975 $p<0.001$ = ***.
976

Table1: List of anti-spike antibodies used in this study. n.d.: Not determined; N/A: Not applicable

Spike region	International Nonproprietary Names	Code mAb	Epitope	Reference
Anti-RBD	Bamlanivimab	BAM	Class Ia	Jones B. et al., Sci Transl Med, 2021
	Imdevimab	IMD	Class Ia	Hansen J. et al., Science, 2020
	Cilgavimab	CIL	Class Ia	Zost S.J. et al., Nature, 2020
	Sotrovimab	S309	Class Ia	Pinto D. et al., Nature, 2020
	Tixagevimab	TIX	Class Ia/Ib	Zost S.J. et al., Nature, 2020
	Bebteloviamb	LyCoV-1404	Class Ia/Ib	Westendorf K. et al., Cell Rep, 2022
	Casirivimab	CAS	Class Ib	Hansen J. et al., Science, 2020
	N/A	SA55	Class I	Cao Y. et al., Cel Rep, 2022
	Etesevimab	ETE	Class Ia/IIa	Shi R. Nature, 2020
	Adintrevimab	ADG2	Class I/IV	Rappazzo C.G. et al., Science, 2021
	Regdanvimab	REG	Class IV	Kim C. et al., Nat Comm, 2021
	N/A	2-43	Trimer interface	Liu L. et al., Nature, 2020
Anti-NTD	N/A	Cv2.5105	Non-supersite	Planchais C. et al. *J Exp Med* 2022
	N/A	Cv2.1153	Non-supersite	Planchais C. et al. *J Exp Med* 2022
	N/A	Cv2.1191	Non-supersite	Planchais C. et al. *J Exp Med* 2022
	N/A	Cv2.3144	Non-supersite	Planchais C. et al. *J Exp Med* 2022
	N/A	Cv2.1309	Non-supersite	Planchais C. et al. *J Exp Med* 2022
	N/A	Cv2.2333	Non-supersite	Planchais C. et al. *J Exp Med* 2022
	N/A	Cv2.2396	Non-supersite	Planchais C. et al. *J Exp Med* 2022
	N/A	Cv2.1177	Supersite	Planchais C. et al. *J Exp Med* 2022
	N/A	Cv2.2221	Supersite	Planchais C. et al. *J Exp Med* 2022
	N/A	Cv2.3215	Supersite	Planchais C. et al. *J Exp Med* 2022
	N/A	Cv2.3296	Supersite	Planchais C. et al. *J Exp Med* 2022
	N/A	Cv2.8145	Supersite	Planchais C. et al. *J Exp Med* 2022
	N/A	Cv2.8162	Supersite	Planchais C. et al. *J Exp Med* 2022
	N/A	Cv2.2157	Supersite	Planchais C. et al. *J Exp Med* 2022
	N/A	Cv2.1177	Supersite	Planchais C. et al. *J Exp Med* 2022
	N/A	Cv2.1169	n.d.	Planchais C. et al. *J Exp Med* 2022
Anti-S2	N/A	Cv2.2180	n.d.	Planchais C. et al. *J Exp Med* 2022
	N/A	Cv2.2216	n.d.	Planchais C. et al. *J Exp Med* 2022
	N/A	Cv2.8187	n.d.	Planchais C. et al. *J Exp Med* 2022
	N/A	Cv2.4102	n.d.	Planchais C. et al. *J Exp Med* 2022
	N/A	Cv2.1380	n.d.	Planchais C. et al. *J Exp Med* 2022
	N/A	Cv2.3175	n.d.	Planchais C. et al. *J Exp Med* 2022
	N/A	Cv2.4171	n.d.	Planchais C. et al. *J Exp Med* 2022
	N/A	Cv2.9116	n.d.	Planchais C. et al. *J Exp Med* 2022
	N/A	Cv2.3132	Heptad repeat 2 (HR2)	Planchais C. et al. *iScience 2024*
	N/A	CoV44-62	Fusion peptide	Dacon C. et al. *Science* 2022
	N/A	76E1	Fusion peptide	Sun X. et al. *Nat. Microbiol.* 2022
	N/A	C77G12	Fusion peptide	Low S. et al. Science 2022
n	39			

Table 2: Patients characteristics of which serum were used for this study. Individuals received Pfizer-BioNTech COVID-19 vaccine (BNT162b2) and were admitted in Lyon Hospice Civils for COVID-19 infection. Autoimmune and inflammatory disease include: Adisson's disease, Celiac disease, and Crohn's disease.

n	15
Age at blood sampling (years), median [IQR]	55 [28–61]
Female, *n* (%)	12 (80)
Time elapsed between the last vaccination or infection event and blood sampling (days)	110 [94–112]
Body mass index, n	15/15
Body mass index, median [IQR]	23.88 [20.20–27.72]
Currently smoker, *n* (%)	1/15 (6.66)
Alcohol consumption (daily), n (%)	0/15 (0)
Comorbidities	
Presence of comorbidities, *n* (%)	3/15 (20)
Neurological disorders, *n* (%)	1 (6.66)
Cardiovascular disorders, n (%)	1 (6.66)
Hypertension, *n* (%)	0 (0)
Heart failure, *n* (%)	0 (0)
Diabetes, *n* (%)	0 (0)
Immune deficiency, *n* (%)	0 (0)
Liver disease, *n* (%)	0 (0)
Kidney disease, *n* (%)	0 (0)
History of cancer, *n* (%)	0 (0)
Hypothyroidy, *n* (%)	0 (0)
Rheumatic disease, *n* (%)	1 (6.66)
Chronic lung disease, *n* (%)	1 (6.66)
Autoimmune and inflammatory disease, n (%)	0 (0)

979

980

Figure 1

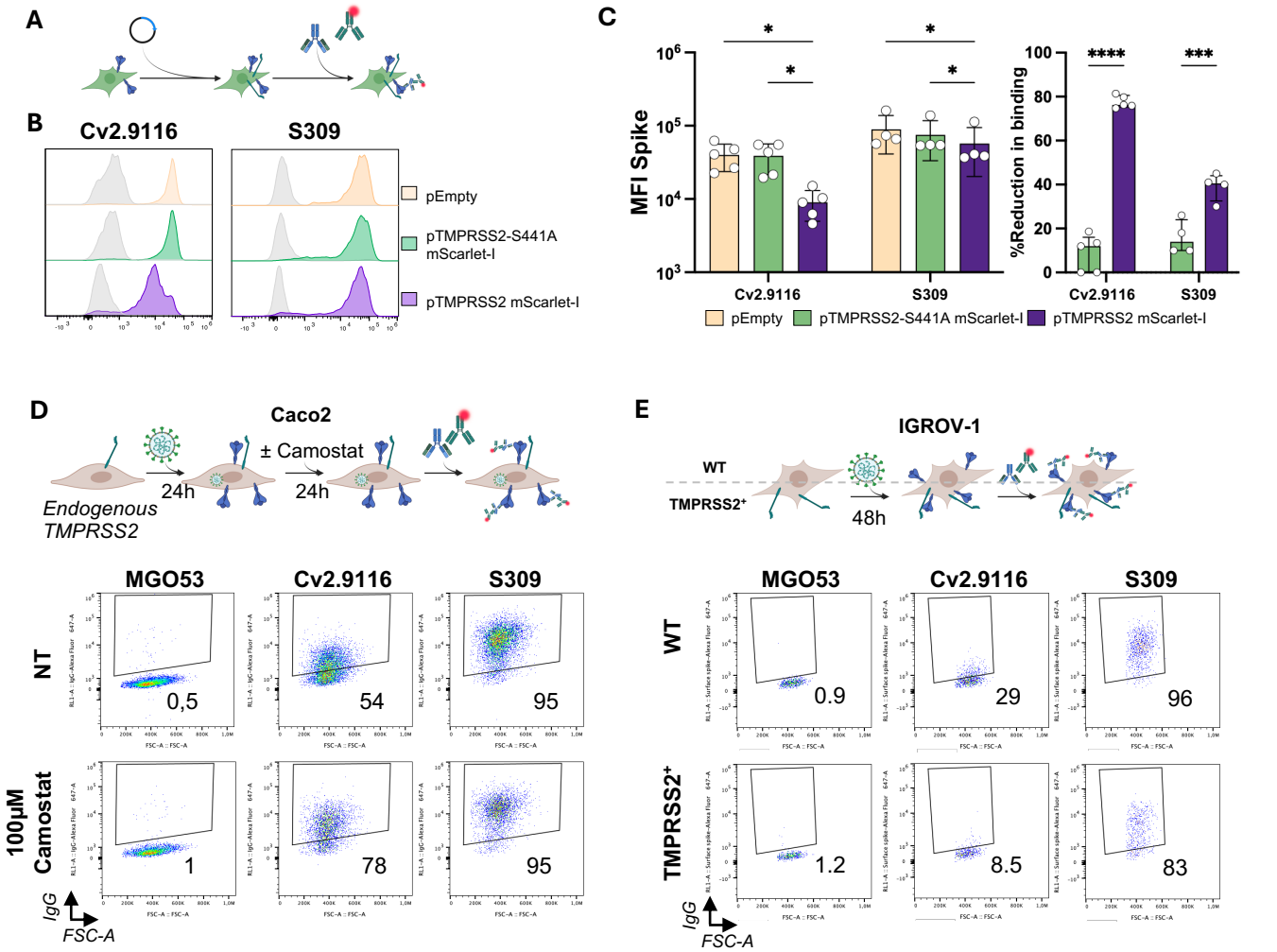
A
B
Cv2.9116
S309
pEmpty
pTMPRSS2-S441A mScarlet-I
pTMPRSS2 mScarlet-I
C
MFI Spike
%Reduction in binding
Cv2.9116
S309
pEmpty
pTMPRSS2-S441A mScarlet-I
pTMPRSS2 mScarlet-I
D
Caco2
± Camostat
24h
24h
Endogenous TMPRSS2
MGO53
Cv2.9116
S309
NT
100µM Camostat
0,5
54
95
1
78
95
IgG
FSC-A
E
IGROV-1
WT
TMPRSS2+
48h
MGO53
Cv2.9116
S309
WT
TMPRSS2+
0.9
29
96
1.2
8.5
83
IgG
FSC-A

Figure 2

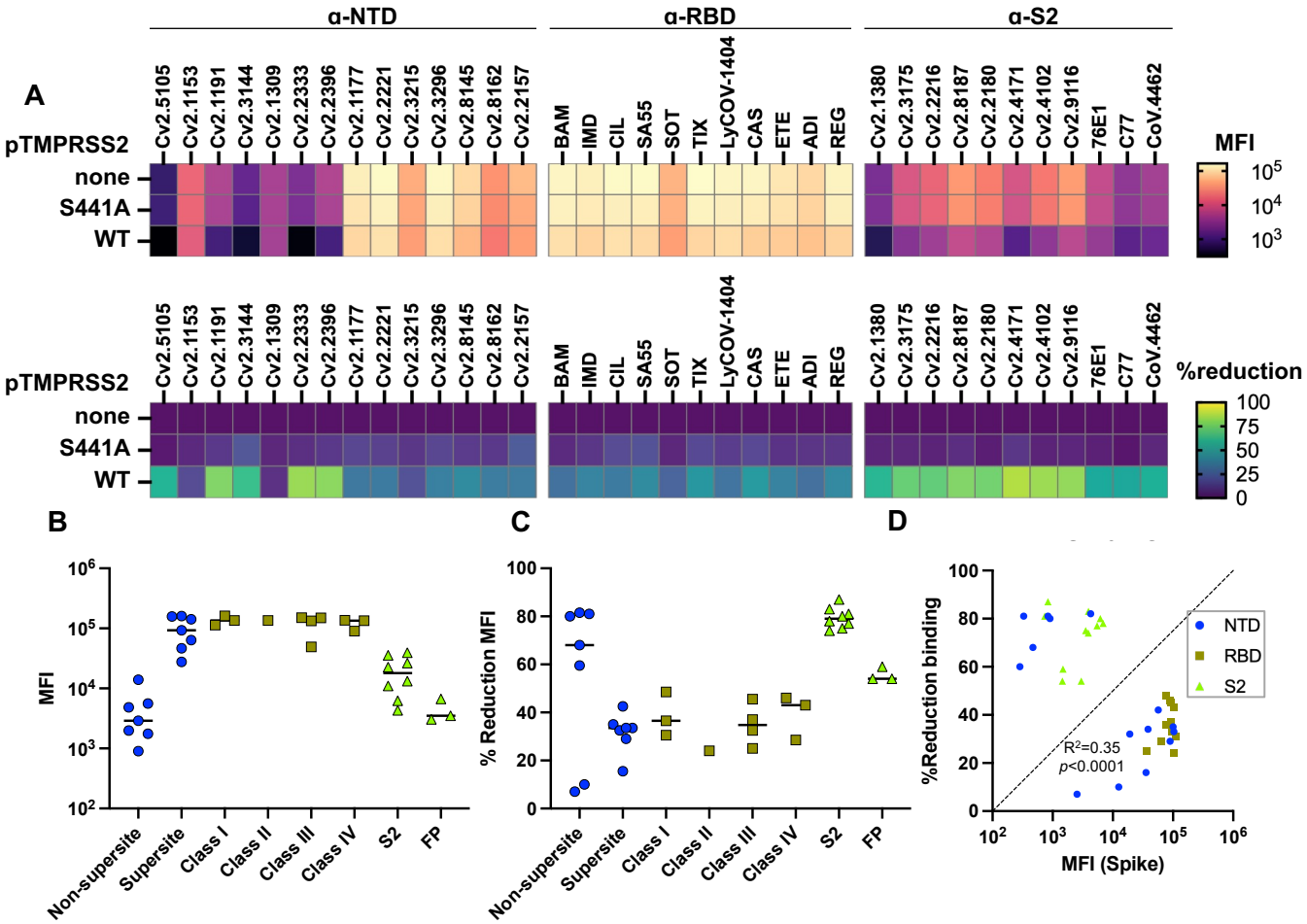
A
α-NTD
α-RBD
α-S2
pTMPRSS2
none
S441A
WT
Cv2.5105
Cv2.1153
Cv2.1191
Cv2.3144
Cv2.1309
Cv2.2333
Cv2.2396
Cv2.1177
Cv2.2221
Cv2.3215
Cv2.3296
Cv2.8145
Cv2.8162
Cv2.2157
BAM
IMD
CIL
SA55
SOT
TIX
LyCOV-1404
CAS
ETE
ADI
REG
Cv2.1380
Cv2.3175
Cv2.2216
Cv2.8187
Cv2.2180
Cv2.4171
Cv2.4102
Cv2.9116
76E1
C77
CoV.4462
MFI
%reduction
B
C
D
MFI
% Reduction MFI
%Reduction binding
MFI (Spike)
Non-supersite
Supersite
Class I
Class II
Class III
Class IV
S2
FP
NTD
RBD
S2
R²=0.35
p<0.0001

Figure 3

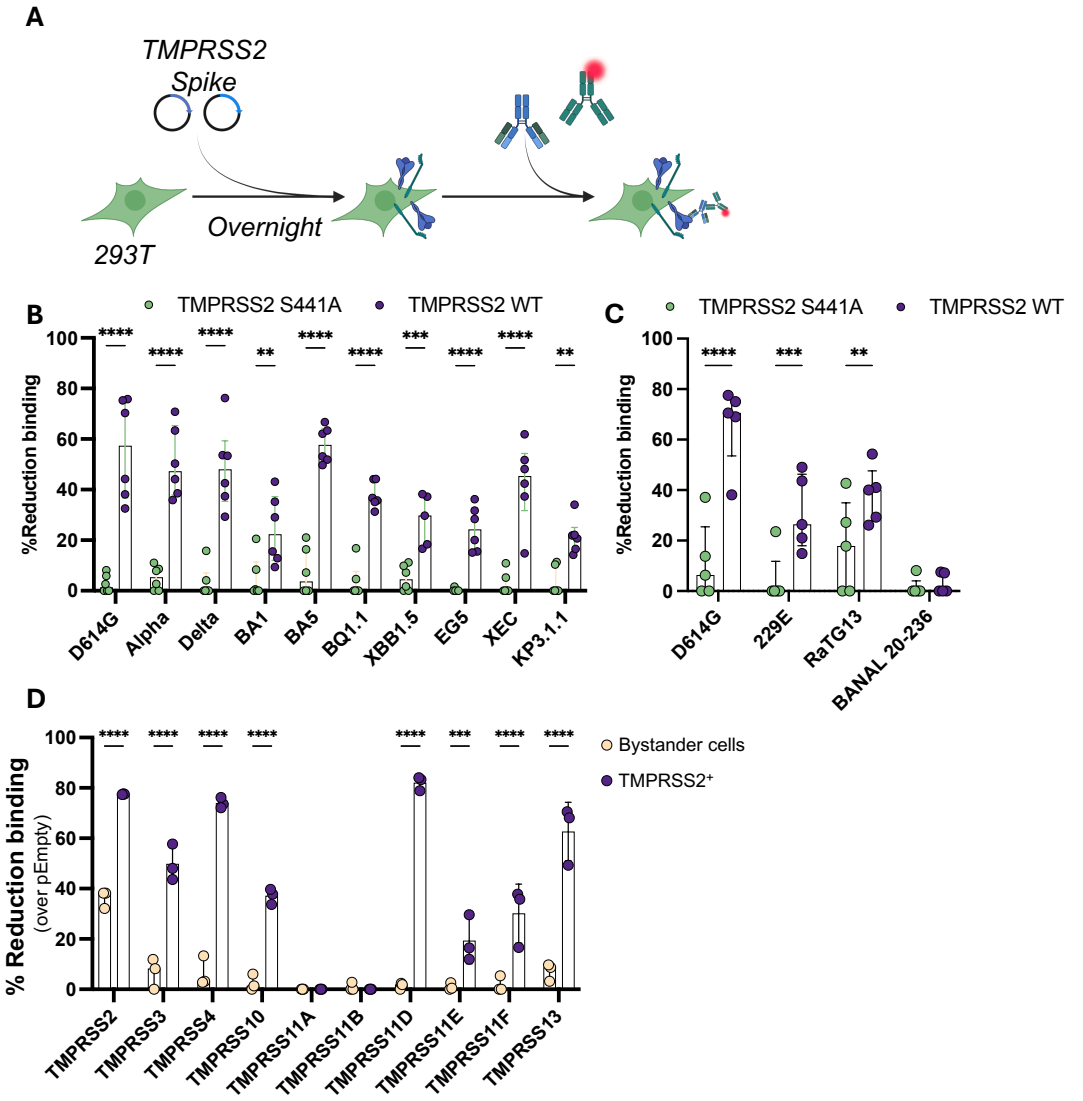
A
TMPRSS2
Spike
293T
Overnight
B
TMPRSS2 S441A
TMPRSS2 WT
%Reduction binding
D614G
Alpha
Delta
BA1
BA5
BQ1.1
XBB1.5
EG5
XEC
KP3.1.1
C
229E
RaTG13
BANAL 20-236
D
% Reduction binding
(over pEmpty)
Bystander cells
TMPRSS2+
TMPRSS2
TMPRSS3
TMPRSS4
TMPRSS10
TMPRSS11A
TMPRSS11B
TMPRSS11D
TMPRSS11E
TMPRSS11F
TMPRSS13

Figure 4

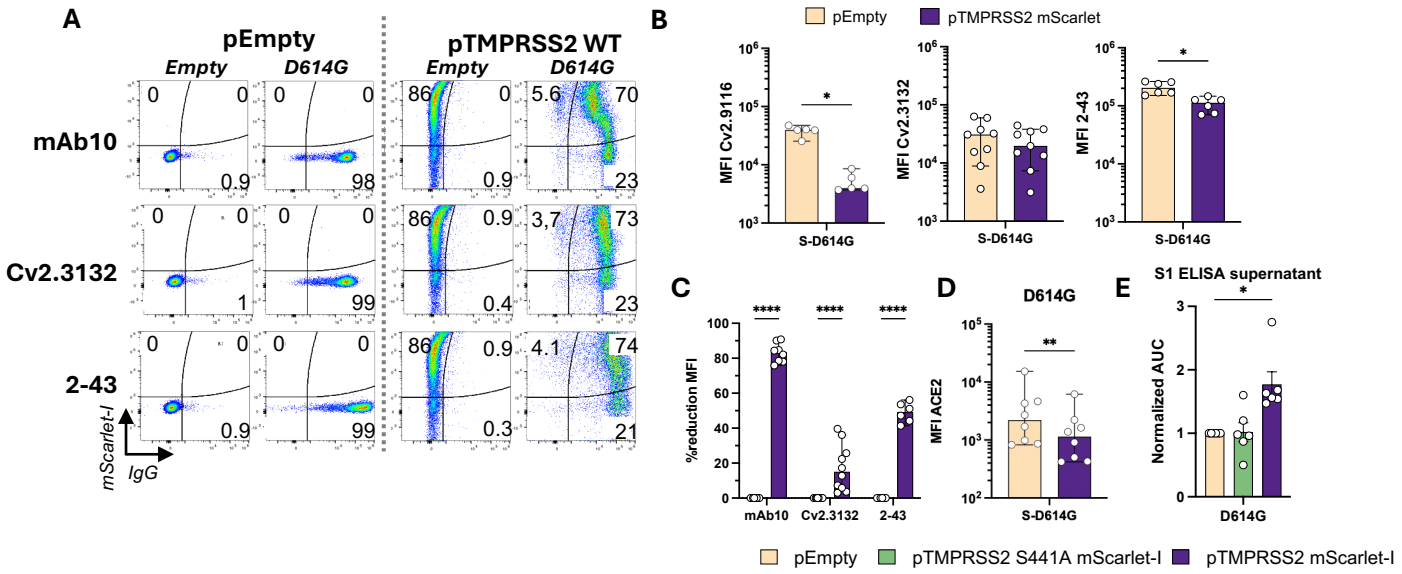
A
pEmpty
pTMPRSS2 WT
Empty
D614G
Empty
D614G
mAb10
Cv2.3132
2-43
mScarlet-I
IgG
B
pEmpty
pTMPRSS2 mScarlet
MFI Cv2.9116
MFI Cv2.3132
MFI 2-43
S-D614G
C
%reduction MFI
mAb10
Cv2.3132
2-43
D
D614G
MFI ACE2
S-D614G
E
S1 ELISA supernatant
Normalized AUC
D614G
pEmpty
pTMPRSS2 S441A mScarlet-I
pTMPRSS2 mScarlet-I

Figure 5

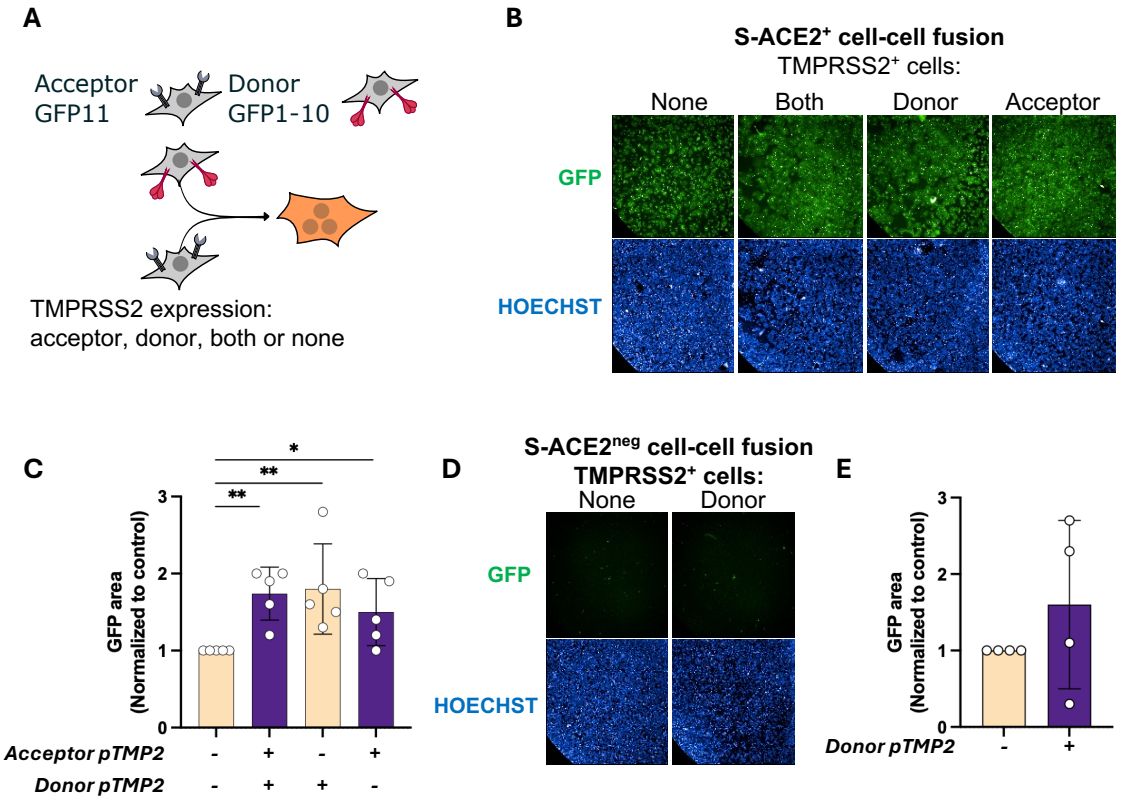
A
Acceptor
GFP11
Donor
GFP1-10
TMPRSS2 expression:
acceptor, donor, both or none
B
S-ACE2+ cell-cell fusion
TMPRSS2+ cells:
None
Both
Donor
Acceptor
GFP
HOECHST
C
GFP area
(Normalized to control)
Acceptor pTMP2
Donor pTMP2
D
S-ACE2neg cell-cell fusion
TMPRSS2+ cells:
None
Donor
GFP
HOECHST
E
GFP area
(Normalized to control)
Donor pTMP2

Figure 6

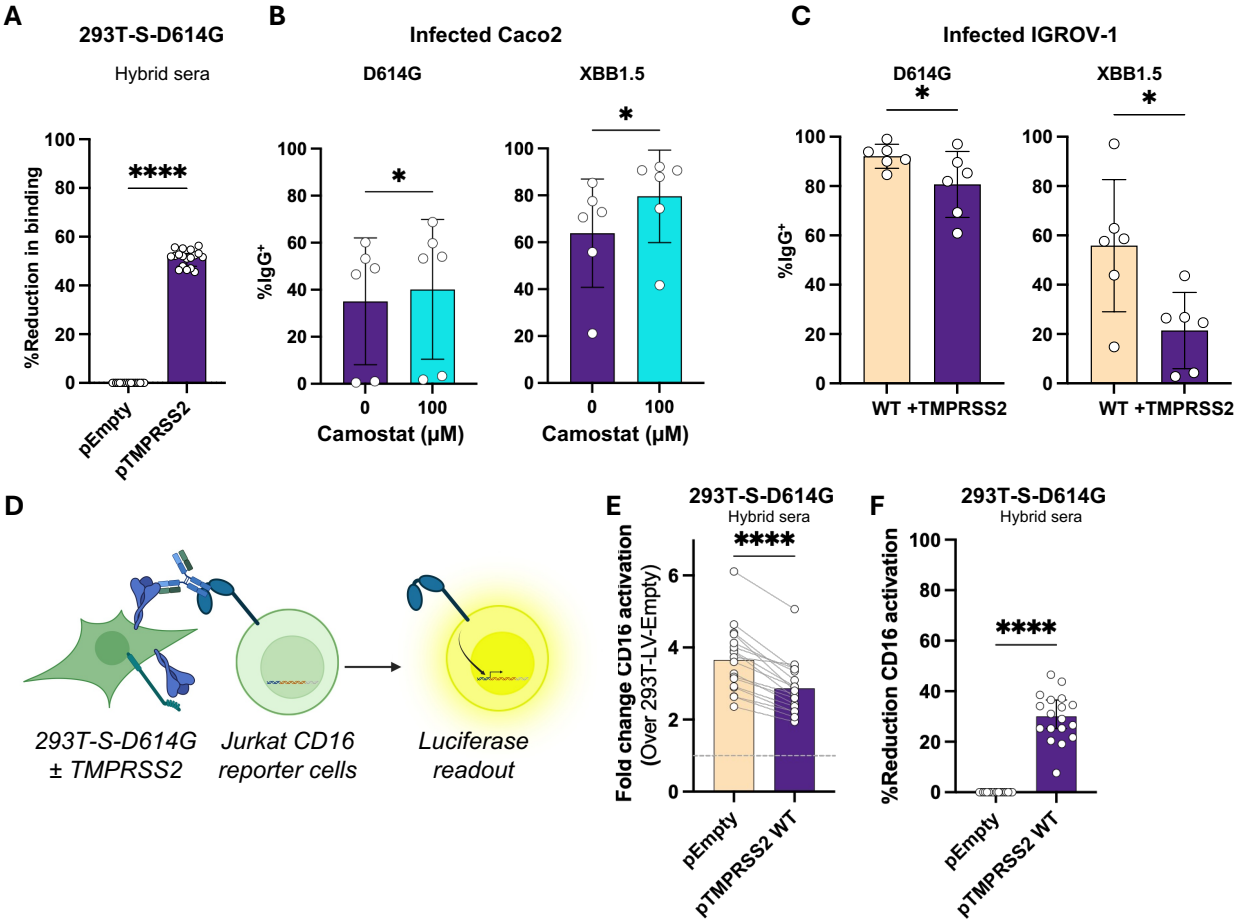
A
293T-S-D614G
Hybrid sera
%Reduction in binding
****
pEmpty
pTMPRSS2
B
Infected Caco2
D614G
XBB1.5
%IgG+
*
*
Camostat (μM)
Camostat (μM)
C
Infected IGROV-1
D614G
XBB1.5
%IgG+
*
*
WT
+TMPRSS2
WT
+TMPRSS2
D
293T-S-D614G
± TMPRSS2
Jurkat CD16
reporter cells
Luciferase
readout
E
293T-S-D614G
Hybrid sera
Fold change CD16 activation
(Over 293T-LV-Empty)
****
pEmpty
pTMPRSS2 WT
F
293T-S-D614G
Hybrid sera
%Reduction CD16 activation
****
pEmpty
pTMPRSS2 WT

Figure 7

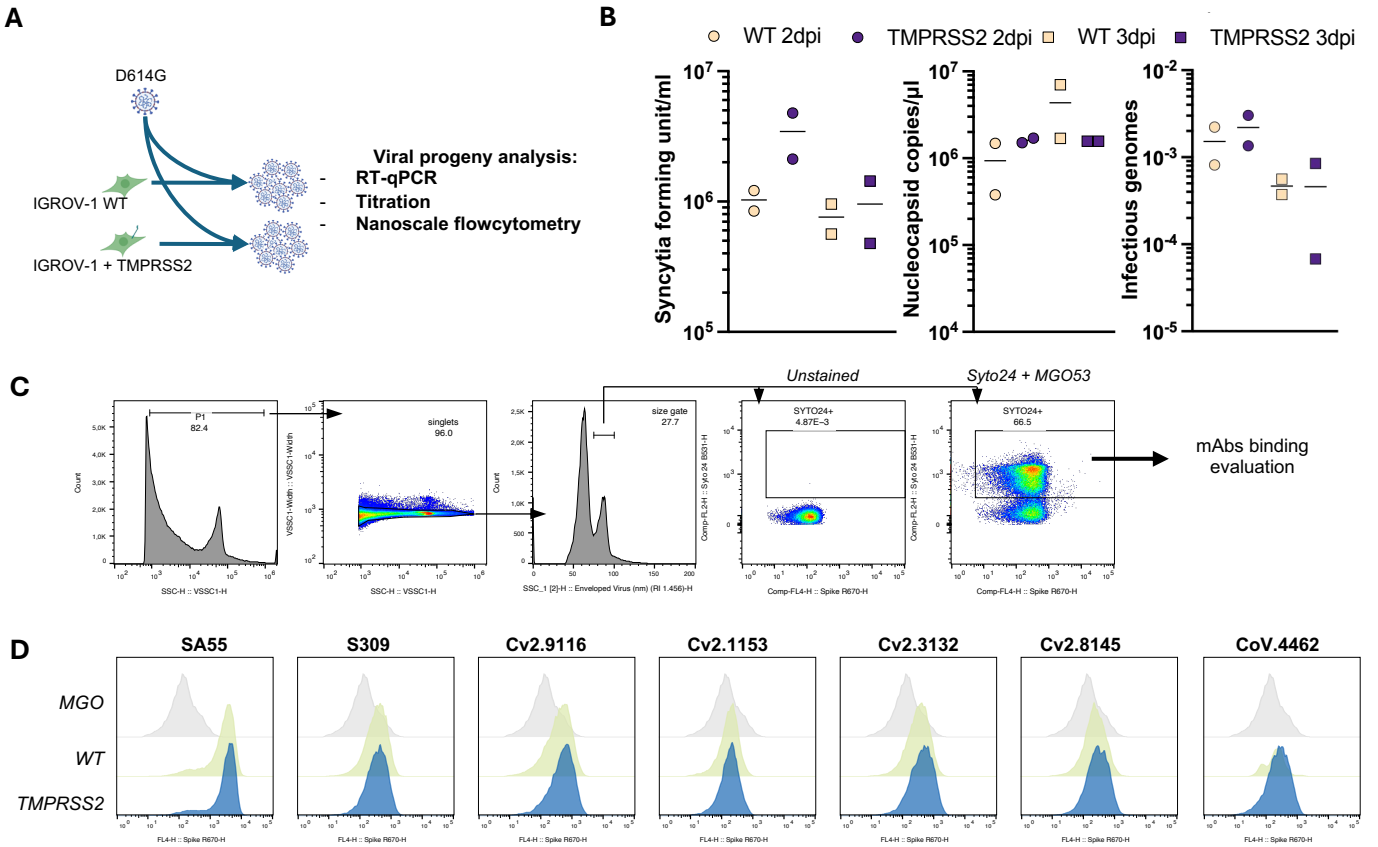
A
D614G
IGROV-1 WT
IGROV-1 + TMPRSS2
Viral progeny analysis:
- RT-qPCR
- Titration
- Nanoscale flowcytometry
B
WT 2dpi
TMPRSS2 2dpi
WT 3dpi
TMPRSS2 3dpi
Syncytia forming unit/ml
Nucleocapsid copies/µl
Infectious genomes
C
Unstained
Syto24 + MGO53
P1
82.4
singlets
96.0
size gate
27.7
SYTO24+
4.87E−3
SYTO24+
66.5
mAbs binding evaluation
D
SA55
S309
Cv2.9116
Cv2.1153
Cv2.3132
Cv2.8145
CoV.4462
MGO
WT
TMPRSS2